JGR Oceans

RESEARCH ARTICLE
10.1029/2022JC018913

# Spatial Variability of Turbulent Mixing From an Underwater Glider in a Large, Deep, Stratified Lake

**Oscar Sepúlveda Steiner[1,2], Alexander L. Forrest[3,4], Jasmin B. T. McInerney[3,4], Bieito Fernández Castro[2,5], Sébastien Lavanchy[2], Alfred Wüest[1,2], and Damien Bouffard[1,6]**

[1]Eawag, Swiss Federal Institute of Aquatic Science and Technology, Surface Waters – Research and Management, Kastanienbaum, Switzerland, [2]Physics of Aquatic Systems Laboratory, Margaretha Kamprad Chair, Institute of Environmental Engineering, ENAC, École Polytechnique Fédérale de Lausanne, Lausanne, Switzerland, [3]Civil & Environmental Engineering, University of California – Davis, Davis, CA, USA, [4]UC Davis Tahoe Environmental Research Center, Incline Village, NV, USA, [5]Ocean and Earth Science, National Oceanography Centre, University of Southampton, Southampton, UK, [6]Institute of Earth Surface Dynamics, University of Lausanne, Quartier Mouline, Lausanne, Switzerland

**Abstract** Recent efforts using microstructure turbulence measurements have contributed to our understanding of the overall energy budget in lakes and linkages to vertical fluxes. A paucity of lake-wide turbulence measurements hinders our ability to assess how representative such budgets are at the basin scale. Using an autonomous underwater glider equipped with a microstructure payload, we explored the spatial variability of turbulence in pelagic and near-shore regions of Lake Geneva. Dissipation rates of kinetic energy and thermal variance were estimated by fitting temperature gradient fluctuations spectra to the Batchelor spectrum. In deep waters, turbulent dissipation rates in the surface and thermocline were mild ($\sim 10^{-8}$ W kg$^{-1}$) and weakened toward the hypolimnion ($\sim 10^{-11}$ to $10^{-10}$ W kg$^{-1}$). The seasonal thermocline exhibited inhibited interior mixing, with extremely low values of mixing efficiency ($Ri_f \ll 0.1$). In contrast, in the slope zone, a band of significantly enhanced energy dissipation ($\sim 5 \times 10^{-8}$ W kg$^{-1}$) extended well above the bottom boundary layer and was associated with strong, efficient mixing ($Ri_f > 0.17$). The resulting contribution of the slope region to basin-scale mixing was large, with 90% of the basin-wide mixing—and only 30% energy dissipation—occurring within 4 km of the shoreline. This boundary mixing will modify overturning circulation and the transport pathways of dissolved compounds exchanged with the sediments. The dynamics responsible for the shift in the mixing regime, which appears crucial for the mixing budget of lakes, could not be fully unraveled with the collected observations. Additional model data analyses hint at the role of submesoscale instabilities.

**Plain Language Summary** Estimating the distribution of kinetic energy in lakes with its associated ecological implications remains challenging due to a lack of lake-wide turbulence measurements. We show that underwater gliders can address this gap by reliably mapping turbulent mixing across broad areas between near-shore and deep-water regions of lakes. Results reveal differences in turbulence intensity and mixing between the interior and coastal zones of deep Lake Geneva (Switzerland/France). Away from the shore, measurements show that (a) the variation in turbulent kinetic energy dissipation is a vertically driven process, and (b) a seasonal thermocline exhibiting little to no turbulent mixing contrary to expectations for such a large, windy lake. Glider measurements along the coastal slope closer to the shore, by contrast, show horizontally resolved turbulent variation within a frictional zone above the slope, far exceeding known values. Moreover, mixing in the near-shore area was enhanced and more efficient than in open waters. This enhanced boundary mixing modifies circulation patterns across lakes and will also influence the exchange of nutrients and dissolved compounds at the sediment-water interface. Our findings highlight the significant variability in turbulence characteristics occurring in lakes and stress the need for gliders to advance our knowledge of physical lake processes.

**Key Points:**

- Underwater gliders are reliable platforms for scanning the spatial heterogeneity and estimating turbulent dissipation in large lakes
- Glider-based temperature microstructure turbulence estimates in the pelagic region reveal inhibited mixing at the seasonal thermocline
- A near-shore glider transect shows a consistent enhancement of turbulent dissipation and buoyancy flux along the sloping bottom surroundings

**Supporting Information:**

Supporting Information may be found in the online version of this article.

**Correspondence to:**

O. Sepúlveda Steiner,
oscar.sepulvedasteiner@eawag.ch

**Citation:**

Sepúlveda Steiner, O., Forrest, A. L., McInerney, J. B. T., Fernández Castro, B., Lavanchy, S., Wüest, A., & Bouffard, D. (2023). Spatial variability of turbulent mixing from an underwater glider in a large, deep, stratified lake. *Journal of Geophysical Research: Oceans*, *128*, e2022JC018913. https://doi.org/10.1029/2022JC018913

Received 27 MAY 2022
Accepted 22 MAY 2023
Corrected 21 JUN 2023

This article was corrected on 21 JUN 2023. See the end of the full text for details.



## 1. Introduction

Climate change is modifying the thermal structure of lakes through increasing surface water temperatures and strengthening seasonal stratification (Adrian et al., 2009; Sahoo et al., 2016; Schwefel et al., 2016). Increased stratification in future climate scenarios will diminish vertical transport and ecologically-relevant exchanges such as oxygen and nutrients renewal will rely primarily on three-dimensional (3D) hydrodynamic processes. The

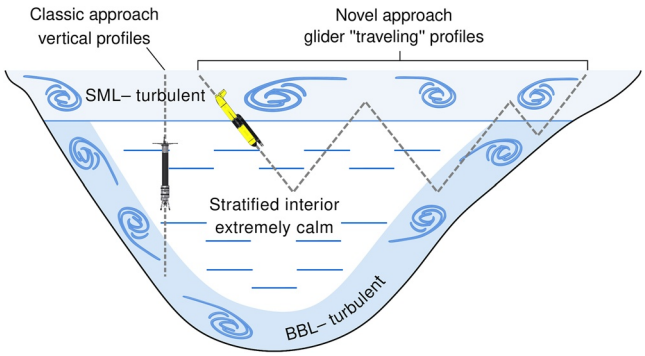


**Figure 1.** Schematics of spatial variability of turbulence intensity in a stratified lake. The sketch depicts turbulence microstructure measurements from a free-falling profiler and an underwater glider transect. Adapted and spatially extended from Wüest and Lorke (2003).

spatial variability of physical properties induced by these processes and, in particular, their link to energy distribution remains poorly studied. A better understanding of lake-wide turbulent mixing can help connect these interactions and ultimately foster our ability to assess the effects of climate change on lake ecosystems.

The pathway of energy transference across scales (i.e., the energy cascade) is a key concept to assess the impacts of atmospheric forcing on the spatial variability of the physical properties of standing water bodies. External forcing transfers energy to large-scale motions providing turbulent kinetic energy (TKE) and inducing broad spatial variability across the entire system. TKE then cascades to smaller scales until it dissipates by friction, mainly at the boundaries (Imberger, 1998). Turbulence microstructure measurements have unraveled the contributions of the interior and boundary regions for the overall kinetic energy budget in the hypolimnion of lakes (Fernández Castro, Bouffard, et al., 2021; Wüest et al., 2000). How representative these budgets are at the spatial extent, particularly for large lakes that exhibit substantial turbulence characteristics differences at relatively short distances of few kilometers (e.g., Bouffard et al., 2012; Lemckert et al., 2004), remains largely unknown.

In medium-to-large lakes, wind and Earth rotation's combined effect are a significant source of large scale processes that drive spatial variability (Csanady, 1975). Complex basin-scale processes such as coastal upwelling (Reiss et al., 2020; Roberts et al., 2021; Schladow et al., 2004), gyres (Ishikawa et al., 2002; Laval et al., 2005; Shimizu et al., 2007), and rotational internal waves (Antenucci et al., 2000; Appt et al., 2004; Bouffard et al., 2012), drive transport and stirring at a wide range of scales. Consequently, these processes will redistribute energy through the generation of turbulence and mixing. Characterizing the in situ spatial variability ranging from basin-scale processes to small-scale turbulence is essential to assess lake-wide energy budgets.

Spatially distributed measurements are required to characterize the spatial heterogeneity of physical and biogeochemical processes. Manual observations of spatial variability such as Conductivity-Temperature-Depth (CTD) transects (Alexander & Imberger, 2013; MacIntyre et al., 2002, 2014) and piloted submarine-based measurements (Fer et al., 2002; Gargett et al., 1984; Osborn & Lueck, 1985; Thorpe et al., 1999) have successfully been applied. However, these applications are logistically and financially prohibitive. Novel autonomous measuring platforms such as self-propelled Autonomous Underwater Vehicles (AUVs; Forrest et al., 2008; Laval et al., 2000) and underwater gliders (Rudnick, 2016; Webb et al., 2001) enable the coupled scanning of vertical and horizontal gradients of water properties with fewer restrictions. The variety of sensors integrated into underwater vehicles, including CTDs and water quality sensors, makes them a suitable platform for studying spatial variability.

Buoyancy-controlled autonomous underwater vehicles (aka gliders) provide “yo-yo” transects through the water column (Davis et al., 2002) with low levels of vibration and mechanical noise critical for making robust turbulence measurements. Microstructure-based turbulence estimates using gliders have been tested in deep oceanic environments featuring energetic (Fer et al., 2014; Peterson & Fer, 2014) and weak (Scheifele et al., 2018) regimes as well as in the upper ocean (Lucas et al., 2019) and shallow shelf seas (Schultze et al., 2017). Although the potential for underwater glider deployments in lakes has been previously identified (Austin, 2013), their application has been slow to manifest (Austin, 2012, 2019; McInerney et al., 2019) and we still lack a clear assessment of the potential of glider-based turbulence observations in lakes. The aim of this work is to provide insight into the spatial distribution of turbulent quantities in lakes' interior and coastal regions using underwater glider measurements (Figure 1).

In the present study, we explore turbulence characteristics of distinct lake regions using an underwater glider. To this end, we first validated temperature microstructure turbulence estimates from a moving platform in a weakly energetic system. With this technical barrier solved, we present a large and novel dataset of glider-based turbulent mixing in the interior and coastal regions of a large, deep, stratified lake. We carry out two analyses of turbulent mixing. First, we use the lake interior results (five [5] missions) to evaluate turbulent mixing parameterizations in this region and discuss particular aspects of strongly stratified and weakly energetic systems. Second, we focus

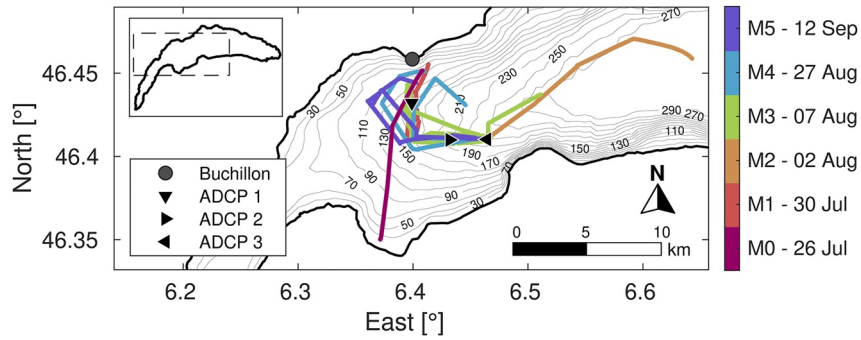


**Figure 2.** Study site location. Bathymetry of Lake Geneva (Switzerland/France) with the location of the Buchillon station and the three moorings (ADCP 1 to 3). Color-coded lines depict glider missions M0 to M5, respectively. Dates correspond to the year 2018.

on the interior-coastal transition region, where our measurements revealed consistent turbulence and mixing enhancement along the slope (one [1] mission). As glider measurements alone cannot explain this feature, we discuss possible hydrodynamic processes driving turbulent mixing at slopes.

## 2. Study Site

This study was conducted on Lake Geneva (*Lac Léman*; Figure 2), a deep (309 m max. depth) and large (582 km$^2$ surface area) perialpine lake located between Switzerland and France. Lake Geneva is the largest natural freshwater body in Western Europe and is classified as a warm-monomictic lake where complete deep winter mixing seldomly occurs (Schwefel et al., 2016). During the seasonal stratification, the thermocline is located at ∼5 to ∼10 m depth in May and gradually deepens during summer and autumn before deep winter convective mixing sets in. The wind is the driving force for horizontal water mass movements (Bohle-Carbonell, 1986), exhibiting two dominant winds: North-East (*La Bise*) and South-West (*Le Vent*; Lemmin & D'Adamo, 1996). Previous studies highlight the role of Coriolis forcing in the dynamics of Lake Geneva (Bauer et al., 1981; Lemmin et al., 2005; Reiss et al., 2020). This forcing will play a particular role during summer stratified conditions, when the maximum width of the lake (∼14 km) is more than three times larger than the internal Rossby radius (∼4 km; Bouffard & Lemmin, 2013a). Past studies of turbulence in Lake Geneva have mainly focused on the near-shore region. Cooling-driven gravity currents (Fer et al., 2002) and internal Kelvin wave-induced shear (Bouffard & Lemmin, 2013b; Thorpe et al., 1999) cause localized and intermittent enhancements of turbulent dissipation. In the lake interior, Michalski and Lemmin (1995) used bulk methods (e.g., Jassby & Powell, 1975) to estimate diffusivity from monthly temperature profiles, finding values well above molecular levels (i.e., turbulent mixing) in the upper hypolimnion (down to ∼90 m depth). Instantaneous microstructure turbulence measurements in this zone, up to date, have not been reported.

## 3. Measurements and Methods

### 3.1. Slocum Glider and Turbulence Package

Spatially distributed measurements in Lake Geneva were performed during the field campaign of 2018 using the UC Davis glider *Storm Petrel*, a G2 Slocum underwater glider (1,000 m depth; Teledyne Webb Research). The glider payload included a Sea-Bird pumped CTD, Sea-Bird triplet ECO Puck measuring Chlorophyll-*a* fluorescence, turbidity and CDOM and an Aanderaa Optode dissolved oxygen (DO) sensor. Additionally, a MicroRider-1000 turbulence package (Rockland Scientific International) was mounted on top of the glider (Fer et al., 2014) and recorded microstructure turbulent fluctuations. This customized instrument comprised two shear and two temperature microstructure channels sampled at 512 Hz and an inclinometer and an accurate pressure sensor sampled at 64 Hz. The glider with the mounted MicroRider was ballasted in a freshwater pool with water density comparable to lake water.

We collected temperature ($T$) and shear microstructure measurements during our sampling. The focus in this study is on estimations based on temperature for two reasons: firstly, turbulence estimates based on the

**Table 1**
*Details of Instruments Deployed on Each Station (Figure 2)*

| Station | Frequency [kHz] | Ensemble interval [min.] | Installation depth [m] | Bin size [m] |
|---|---|---|---|---|
| Buchillon | 600 | 15 | 38 | 0.75 |
| ADCP 1 | 600 | 10 | 50 | 1.0 |
| ADCP 2 | 600 | 10 | 42 | 1.0 |
| ADCP 3 | 300 | 5 | 46 | 1.0 |

*Note.* Each station was equipped with a Teledyne RD Workhorse Sentinel of the specified frequency. ADCPs 1 to 3 were installed from 25 July to 10 October 2018.

temperature microstructure technique have shown better performance than shear to characterize weak turbulence, as typically encountered in the stratified hypolimnion of lakes (Kocsis et al., 1999) and occasionally in strongly stratified zones of the ocean (Scheifele et al., 2018); secondly, shear microstructure measurements were not always available due to probes becoming damaged after being accidently recovered in fishing nets. The online dataset includes all microstructure measurements for reproducibility and open science purposes (see Data Availability Statement). A substantial amount of turbulence research in lakes (e.g., Bouffard & Boegman, 2013; Imberger & Ivey, 1991; Saggio & Imberger, 2001; Wüest et al., 2000) supports our choice to proceed with temperature microstructure only and is not considered detrimental to the current study.

### 3.2. Glider Transects

*Interior*—Our glider missions were carried out in the western part of the main basin to minimize safety hazards with summer boat activity offshore of Lausanne. The sampling strategy consisted mainly of repeated L-shaped trajectories keeping the glider away from the steep bathymetry along the north shore of the lake (Figure 2). The glider was programmed to perform continuous dives and climbs (downcast and upcast profiles, respectively) between 3 and 100 m depth, reaching the surface every 4 hr for communications and GPS positioning. Although a deep glider (1,000 m depth) is slow at vertical turning points (hereafter referred to also as turns), the adopted sampling strategy enabled a smooth passage through a significant portion of the water column representing a great range of variability and ensuring that turns occur away from the thermocline. The glider was programmed to perform flights with a fixed pitch angle, allowing for battery position adjustments throughout the missions. Still, the battery position remained almost constant during each dive and climb. For this mission design, the glider traveled a distance of ~410–450 m between two dives and performed 9 to 10 yo-yos (dive and climb) during the 4 hr immersion period.

*Coastal transition*—An opportunistic mission from Buchillon toward the Southern shore of the lake (M0; Figure 2) allowed the vehicle to traverse a gentle slope ($\approx 2^o$) into the coastal region. The vehicle's flight parameters were similar to those selected for the interior missions. In particular, the bottom detection system (underwater altimeter) was set with a tolerance of 10 m to the bottom, allowing the glider to adjust the maximum dive depth when approaching zones shallower than 100 m.

### 3.3. Wind and Current Measurements

A hydro-meteorological station located at Buchillon (Figure 2) provided wind speed and direction measurements from a 05,103 Wind Monitor anemometer (Young, USA) installed at 10 m above the water level, and sampling means and gust values every 10 min. We collected current velocity profiles measurements using moored Acoustic Doppler Current Profilers (ADCPs) to complement the glider observations. The deployment was comprised of three suspended upward-looking ADCPs installed in the open water region (Figure 2), in addition to a long-term deployment of a bottom-moored upward-looking ADCP at Buchillon station. Installation of ADCP moorings 1 to 3 consisted of lines equipped with subsurface floats at their uppermost end (~50 m depth). Each ADCP was installed within a frame assembled to the line, 5 m below the float (assuring no signal interference). An acoustic release system was also installed near the lake floor at the base of each mooring to help retrieve the instruments. This setup allowed scanning of the upper part of the water column with a reasonable resolution given the local restriction due to professional fishing in the top 50 m. Table 1 lists information and deployment depths of each of the ADCPs.

### 3.4. Flight Model and Navigation Around Vertical Turning Points

Glider along-path speeds ($U$) are required to perform accurate turbulence estimations. These are used to treat the microstructure data with the Taylor frozen-flow hypothesis (Section 3.5). Nevertheless, the vehicle's speed through water cannot directly be obtained from instrumentation commonly mounted on gliders. We implemented the dynamic flight model for Slocum gliders of Merckelbach et al. (2019) to address this lack of data. Details of the implementation are presented in the Supporting Information (SI; Text S1 and Figure S1 in

Supporting Information S1). The flight model revealed stable flight characteristics during our deployments, with slower along-glider-path speeds for dives (≈0.3 m $s^{-1}$) than for climbs (≈0.4 m $s^{-1}$).

Vertical turning points require particular attention when integrating flight model results into the turbulence estimates procedure. Navigation around turns presents diminished data quality from changes in glider traveling speed (due to pump operation) that may not satisfy the Taylor frozen-flow hypothesis (Fer et al., 2014). Considering mission M0, which additionally scanned shallow near-shore waters, we analyzed glider navigational data for all turning points as a function of time separating deep and near-surface vertical turns (Figure S2 in Supporting Information S1). Comparing this to the flight model indicated that navigation during deep turns was altered 50/100 s before/after the turning point. This corresponds to vertical distances of 2.1–2.2/8.6–8.9 m before/after deep turns (Table S1 in Supporting Information S1). Navigation was altered 2.1–2.5/4.4–4.6 m (30/60 s) before/after near-surface vertical turnings.

We implemented the navigation analysis in the turbulence processing of our measurements. Data around vertical turning points are excluded, as shown for M0. Accordingly, in open waters transects (M1-M5), turbulence analyses exclude data collected 5 m within near-surface turns and 2.5/9.0 m before/after deep turning points.

### 3.5. Turbulent Dissipation From Temperature Microstructure

The possibility to estimate turbulence characteristics from temperature microstructure sensors (fast thermistors) mounted on gliders has already been successfully demonstrated (Peterson & Fer, 2014; Scheifele et al., 2018). Measurements carried out with these sensors can be used to estimate along-glider-path rates of turbulent kinetic energy dissipation, $\varepsilon$ (W $kg^{-1}$), and temperature variance smoothing, $\chi_\theta$ (°$C^2$ $s^{-1}$). This is achieved by fitting the measured temperature gradient spectra ($S_{obs}$) to a theoretical spectral shape $S = S(k_C, \chi_\theta)$, as a function of a cutoff wavenumber ($k_C$) and $\chi_\theta$.

In this work, we adjust $S_{obs}$ to the Batchelor (1959) spectrum, $S_B$, to extract turbulence information from the microstructure data. Performing such spectral fitting allows us to infer $\varepsilon$ estimates (indirectly) because the Batchelor cutoff wavenumber, $k_B$ (cpm), is defined as a function of $\varepsilon$ by:

$$k_B = \frac{1}{2\pi}\left(\frac{\varepsilon}{\nu D_T^2}\right)^{\frac{1}{4}} \tag{1}$$

where $\nu \approx 1.5 \times 10^{-6}$ $m^2$ $s^{-1}$ is the kinematic viscosity and $D_T = 1.4 \times 10^{-7}$ $m^2$ $s^{-1}$ is the molecular thermal diffusion coefficient at hypolimnion temperatures. This data processing employs the maximum likelihood spectral fitting method (Ruddick et al., 2000) to estimate $\varepsilon$, coupled with the Steinbuck et al. (2009) approach to calculate $\chi_\theta$.

The initial step of the procedure is to obtain $S_{obs}$. For this, fast thermistors data are first treated with a double-pole frequency response correction (Sommer et al., 2013). The following data processing is similar to the methodology of Scheifele et al. (2018). However, we use half-overlapping microstructure temperature segments of 10 s to calculate frequency spectra instead of 40 s. Frequency spectra are converted to wavenumber spectra ($S_{obs}$) assuming Taylor's frozen turbulence hypothesis and using 10 s averages of the along-glider-path speed ($\overline{U}$) obtained with the flight model (i.e., $S(k) = \overline{U}S(f)$ with $k = f/\overline{U}$). These deviations from the Scheifele et al. (2018) data treatment allow us to maximize the amount of $S_{obs}$ for turbulence analysis without compromising data quality (see Section 4.2).

Then, the procedure requires obtaining $\chi_\theta$, which is obtained directly through integration of the temperature gradient spectra. We take advantage of the Steinbuck et al. (2009) correction to filter fine-scale fluctuations (Gregg, 1977) and possible low-frequency vehicle-induced contamination by modifying some commonly used parameters (namely $k_l$ and $k_u$ in Equation 2). The calculation of $\chi_\theta$ is performed with the following integral:

$$\chi_\theta = \chi_l + \chi_{obs} + \chi_u = 6D_T\left(\int_o^{k_l} S_B\,dk + \int_{k_l}^{k_u}(S_{obs} - S_n)\,dk + \int_{k_u}^{\infty} S_B\,dk\right) \tag{2}$$

with the factor 6 for assuming isotropy. The lower wavenumber end of the measured spectra ($k_l$) is obtained by considering $k_l = \max\{\min\{k_{obs}\};\ 3k_*\}$, where $k_* = 0.04k_B(D_T/\nu)^{1/2}$ is the so-called transitional wavenumber

separating the inertial and viscous-convective subranges (Dillon & Caldwell, 1980). Whereas the upper wavenumber end ($k_u$) is the intersection of $S_{obs}$ with the noise spectra $S_n$. Outside the range defined by $k_l$ and $k_u$, given the lack of reliability of $S_{obs}$, Steinbuck et al. (2009) propose to use the theoretical expression of $S_B$ to obtain the fringe contributions of $\chi_l$ and $\chi_u$.

By coupling the estimation of $\chi_\theta$ and $S_B$ and solving iteratively for $k_B$, we can finally obtain $\varepsilon$. Dissipation estimates obtained from poorly resolved spectra, which do not comply with the Bachelor fitting, are discarded following the likelihood and mean absolute deviation criteria proposed by Ruddick et al. (2000). The detection floor of $\varepsilon$ based in temperature microstructure is in the range of $10^{-12}$ to $10^{-11}$ W kg$^{-1}$ (Luketina & Imberger, 2001; Steinbuck et al., 2009).

The turbulence estimate procedure is highly dependent on along-glider-path speeds. Away from vertical turning points, the implemented dynamic flight model is expected to yield glider velocity errors smaller than 5% (Merckelbach et al., 2019). The corresponding error in $\chi_\theta$ comes from combining its (isotropic) theoretical form $\left(\chi_\theta \equiv 6D_T\overline{(\partial T'/\partial x)^2}\right)$ with the Taylor frozen flow hypothesis for temperature, yielding $\chi_\theta \propto U^{-2}$. For $\varepsilon$, the glider velocity dependence is dictated by the Batchelor wavenumber (Equation 1), hence, $\varepsilon \propto U^{-4}$. Merckelbach et al. (2019) report ratios of modeled to measured along-glider-path speeds, $(U_{model}/U_{meas})^n$, with $n = 2{,}4$, from comparing their calibrated model results to collocated values measured in-situ with an electromagnetic current sensor. They found mean ratios of 1.1 and 1.2 for $n = 2{,}4$, respectively. Therefore, likely errors in $\chi_\theta$ and $\varepsilon$ due to uncertainties in the along-glider-path speed correspond to 10% and 20%, respectively.

Turbulent quantities often exhibit lognormal character. Statistical analyses presented here thus implement the maximum likelihood estimator (mle) for lognormal distributions (Baker & Gibson, 1987), which reduces the influence of extreme values (see Appendix A). Statistics of mle-means are reported as $\overline{X}_{\text{mle}}$ $[\text{LL}, \text{UL}]_{\text{mle 95\%}}$, with LL and UL the lower and upper limits of the mle-mean 95% confidence interval, respectively. In summary Tables, the intermittency factor (an unbiased estimator of the variance in log-space) is reported inside pointy brackets $\langle\sigma^2_{\text{mle}}\rangle$. Arithmetic means and medians accompanied by standard deviations and sample quantiles are also provided for comparison.

### 3.6. Turbulent Mixing Characteristics

Turbulent heat diffusivity is quantified using the along-glider-path $\chi_\theta$ estimates, following the Osborn and Cox (1972) model given by:

$$K_T = \frac{\chi_\theta}{2\left(\frac{\partial \overline{T}}{\partial z}\right)^2} \tag{3}$$

where $\partial\overline{T}/\partial z$ is the background vertical temperature gradient, obtained by calculating the slope of $T$ in the vertical segment of interest through linear regression.

We use the isotropic version of the Cox number to assess whether turbulent temperature fluctuations also reflect mixing, defined as (Thorpe, 2007):

$$C_x = 3\frac{\overline{\left(\frac{\partial T'}{\partial x}\right)^2}}{\left(\frac{\partial \overline{T}}{\partial z}\right)^2} \tag{4}$$

where $\overline{(\partial T'/\partial x)^2}$ is the temperature fluctuation gradient squared through the along-glider-path coordinate ($x$; as defined in Scheifele et al., 2021). When this ratio is less than 1, stirring-induced temperature fluctuations are smoothed-out by the background temperature gradient, and therefore turbulent mixing is inhibited. Taking advantage of the along-glider-path estimate of $\chi_\theta \equiv 6D_T\overline{(\partial T'/\partial x)^2}$ (isotropic turbulence; Osborn & Cox, 1972) we can compute $C_x$ as:

$$C_x \equiv \frac{\frac{\chi_\theta}{2D_T}}{\left(\frac{\partial \overline{T}}{\partial z}\right)^2} = \frac{K_T}{D_T} \tag{5}$$

with $K_T$ obtained directly from Equation 3.

To characterize the intensity of turbulence with respect to stratification, we use the buoyancy Reynolds number (Gibson, 1980):

$$Re_b = \frac{\varepsilon}{\nu N^2} \tag{6}$$

where $N^2 = g\rho_o^{-1}\partial\rho/\partial z$ is buoyancy frequency squared and represents the water column stability, $g = 9.81$ m s$^{-2}$, and $z$ is the depth coordinate (positive downwards). Freshwater density, $\rho$, is calculated from CTD data using methods ad-hoc with TEOS 2010 (McDougall & Barker, 2011) and $\rho_o = 1{,}000$ kg m$^{-3}$ is the freshwater reference density. The density gradient, $\partial\rho/\partial z$, is obtained through linear regression of $\rho$ in the vertical segment of interest. $Re_b$ is considered to define three energy regimes (Ivey et al., 2008): molecular ($Re_b < 7$), transitional ($7 < Re_b < 100$) and turbulent ($Re_b > 100$).

We use the flux Richardson number, $Ri_f$, to account for mixing efficiency (Monismith et al., 2018). Assuming steady and homogeneous turbulence, the local shear production ($P$) balances with the sum of buoyancy flux and dissipation (i.e., $P = B + \varepsilon$; Ivey & Imberger, 1991). Hence, we can define $Ri_f$ as:

$$Ri_f = \frac{B}{B + \varepsilon} \tag{7}$$

where $B = K_T N^2$ is the buoyancy flux. The flux Richardson number can be rewritten as a function of $C_x$ and $Re_b$ as follows:

$$Ri_f(C_x, Re_b) = \frac{C_x(D_T/\nu)}{C_x(D_T/\nu) + Re_b} \tag{8}$$

Since $Re_b$ defines energy regimes, mixing efficiency studies often consider it the primary controlling parameter (e.g., Bouffard & Boegman, 2013; Monismith et al., 2018). The use of $C_x$, however, remains less explored. In this work, we revisit using $C_x$ to characterize turbulence and mixing (e.g., Dillon & Caldwell, 1980; Smyth & Moum, 2000b).

### 3.7. Horizontal Kinetic Energy and Stirring

Using the ADCP current data allows us to determine the depth-integrated horizontal kinetic energy (HKE):

$$\mathrm{HKE} = \frac{1}{2}\int_0^{z_{\mathrm{ADCP}}} \left(u^2 + v^2\right)\, dz \quad \left(\mathrm{m}^3\,\mathrm{s}^{-2}\right) \tag{9}$$

where $u$ and $v$ are the East and North current components, respectively. The vertical integration range is considered from the surface ($z = 0$ m) to $z_{\mathrm{ADCP}} = 40$ m depth. A characteristic radius resulting from circulation at a specific frequency band ($f^*$) can then be defined as:

$$R^* = \frac{\sqrt{2\overline{\mathrm{HKE}^*}\, z_{\mathrm{ADCP}}^{-1}}}{2\pi f^*} \tag{10}$$

where $\overline{\mathrm{HKE}^*}$ is the mean of the bandpass-filtered HKE at a frequency $f^*$. We use this radius to approximate a scale of horizontal stirring at a specific energy-containing frequency band (e.g., internal waves).

## 4. Results

This research explores the capabilities of underwater gliders for studying spatial variability in a large lake. Glider *Storm Petrel* was deployed in Lake Geneva in the summer of 2018 to connect large-scale spatial variability to turbulence activity. Throughout the six missions considered in this study, we measured 345 yo-yo sets equivalent to 155 hr of sampling, covering a lake surface distance of 158 km. In this section, we present an overview of the data collected by the glider, an assessment of the procedure to obtain turbulence estimates, a comparison of turbulence and mixing conditions between interior and coastal regions of the lake, and the sources of spatial variability

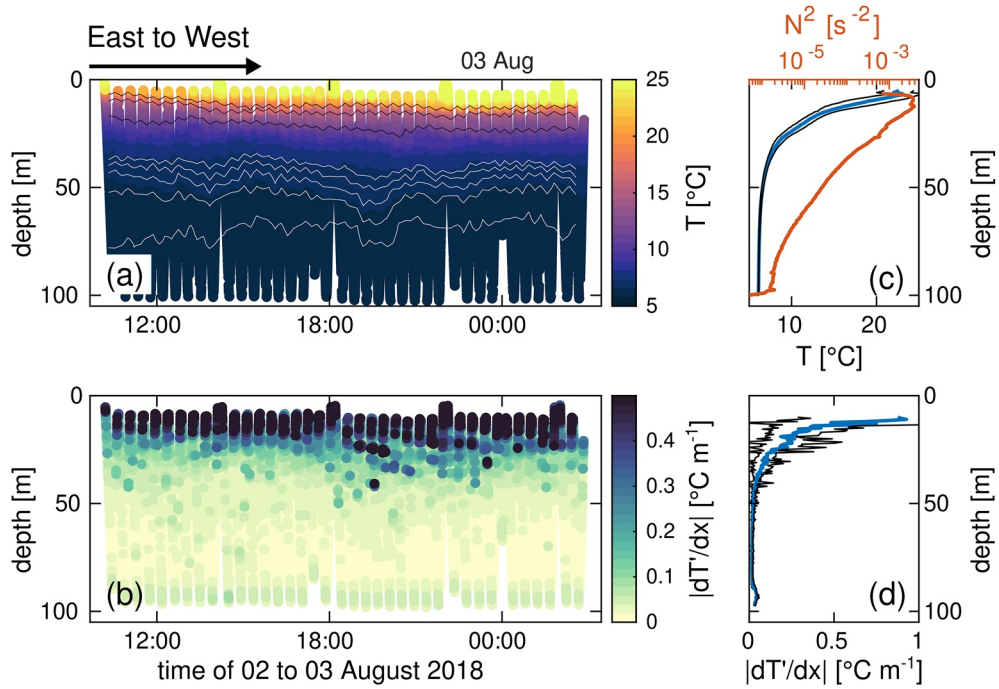


**Figure 3.** Example of lake-interior glider data collected on 2–3 August 2018 during mission M2. (a) Temperature (*T*). (b) Absolute value of 10-s bins along-glider-path temperature fluctuation gradient obtained from applying the Taylor frozen flow hypothesis dT'/dx = (1/U)dT'/dt to the temporal temperature fluctuation gradient dT'/dt directly from the MicroRider and using along-path speeds from the glider flight model. Time increase corresponds to E-W direction (Figure 2). (c)–(d) Time-averaged profiles (blue lines) of measurements presented in (a)–(b), accompanied by their respective standard deviations (black line envelopes). Additionally, (c) shows the averaged stability ($N^2$) profile for mission M2 (red line). Isotherms in (a), gray: 6.2, 6.4, 6.6, 6.8, and 7.0°C; black: 10, 13, and 15°C.

evaluated from wind and ADCP measurements. Glider, MicroRider and ADCP data are available at the following Zenodo repository: Sepúlveda Steiner et al. (2023a).

### 4.1. Glider Measurements

*Interior*—We show a time-series example of data collected during mission M2 (Figures 3a and 3b), consisting of a long transect through the middle of the lake (Figure 2). This and the other interior missions, accompanied by water quality parameters less relevant for the analysis presented herein (namely Chlorophyll-*a* and dissolved oxygen), are presented in the SI (Figures S3–S7 in Supporting Information S1). Mission-composite averaged profiles during M2 show a marked, expected vertical structure (Figures 3c and 3d) with a warmer, seasonal epilimnion overlying the cooler hypolimnion. However, a more careful analysis of the sample transect reveals lateral heterogeneity in the top 50 m with varying thermocline depths (depicted by ~15°C isotherm; Figures 3a and 3b). The first 4 hr of this mission presented colder temperatures close to the surface, suggesting a thermocline uplift in the eastern part of the main basin potentially as a result of localized upwelling. The along-glider-path temperature fluctuation gradient (dT'/dx; Figure 3d), a practical proxy for turbulence, exhibits a vertically consistent decay with horizontal variability (Figure 3b). Sharper fluctuation gradients in the upper water column appropriately reflect turbulence enhancement due to wind forcing, as this region is directly exposed to wind shear at the surface. Similar spatiotemporal variability was observed during other missions (see Figures S3–S7 in Supporting Information S1).

*Coastal transition*—The time series of the cross-shore mission M0 (Figures 4a and 4b) shows similar temperature characteristics as M2. However, the along-glider-path temperature fluctuation gradient shows marked spatial heterogeneity with an enhancement toward the slope. Averaged profiles (Figures 4c and 4d) depict a similar vertical structure as the pelagic profiles with a strong vertical stratification (Figure 4c). Overall, M0 shows a stratified water column with enhanced variability toward the shore, highlighting the different characteristics between

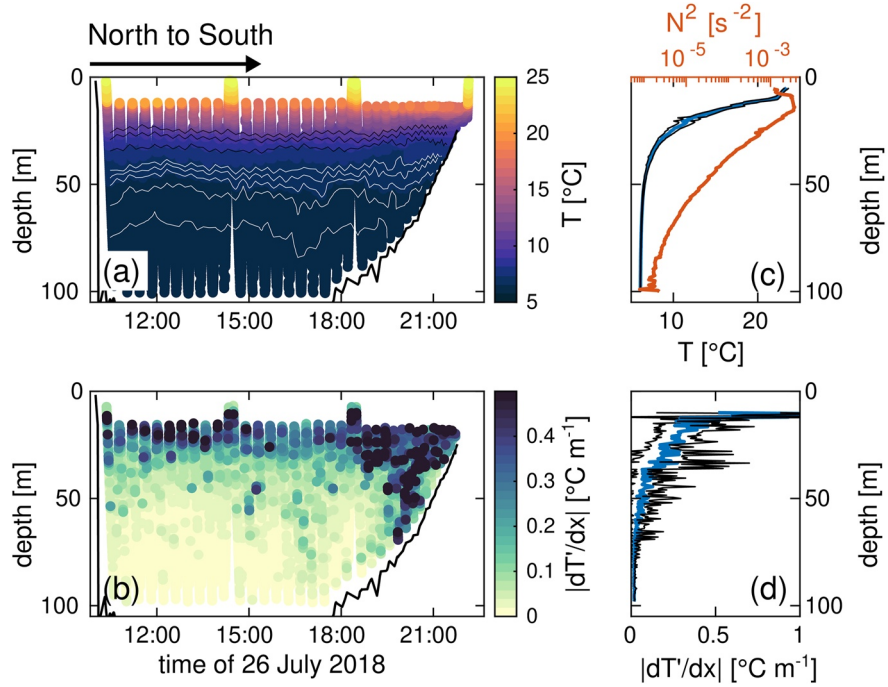


**Figure 4.** Cross-shore (interior-to-coast) glider data collected on 26 July 2018 during mission M0. Panels are analogous to Figure 3. Isotherms in (a), gray: 6.2, 6.4, 6.6, 6.8, and 7.0°C; black: 8, 9, and 10°C. Thick black line in (a) and (b) represents the lake bed as detected by the glider's altimeter.

the interior and coast. Details of the water quality parameters collected during M0 are presented in Figure S8 in Supporting Information S1.

### 4.2. Turbulence Estimates Assessment

To evaluate the microstructure analysis methodology for determining estimates of $\varepsilon$ and $\chi_\theta$ we performed a statistical assessment of the non-dimensional spectral shapes for temperature fluctuations following Dillon and Caldwell (1980). We examine spectra from dives and climbs combined below, while separated analyses are presented in the SI (Figures S9 and S10 in Supporting Information S1). This analysis considers spectra calculated from each fast thermistor as separate samples (no averaging). Figure 5 shows ensemble averages of microstructure temperature gradient spectra that meet the Ruddick et al. (2000) criteria and compare them with $S_B$ for different Cox number ($C_x$) ranges. Considering measurements away from vertical turning points 60% of the 71,903 spectra analyzed were non-compliant with this criterion and therefore discarded. For small $C_x$, that is, when the background temperature gradients are more prominent than those imposed by turbulent fluctuations, spectra present a shape seemingly in disagreement with the Batchelor form in the lower wavenumber range. For wavenumbers above the spectral maximum, observed spectra show, in general, good agreement with $S_B$. This resemblance is evident for a wide range of $C_x$, namely $C_x > 0.1$ (Figures 5c–5f).

The specific evaluation of our procedure to calculate $\chi_\theta$ (Equation 2) requires a careful analysis of the $S_{obs}$ ensembles at their wavenumber extremes (Figure 5). At the upper wavenumber end, the intersection of $S_{obs}$ with $S_n$ defines the cutoff and the maximum likelihood method (Ruddick et al., 2000) prevents an overestimation of $\chi_\theta$ by avoiding the noise-dominated region. For low wavenumbers, the ensemble averages detach from the theoretical form, $S_B$, possibly due to vehicle-induced vibrations and/or stratification fine-scale structures. This deviation becomes evident at the lower wavenumber end of the spectra for $C_x < 10$ (Figure 5a–5d). However, the variance-preserving spectra (circles in Figure 5) show that the statistical variability introduced by $S_{obs}$, not complying with the theoretical $S_B$ shape, affects only wavenumbers below $3\alpha_*$ (where $\alpha_*$ is the non-dimensional form of $k_*$) for $C_x < 0.1$, and it is therefore filtered out during the computation of $\chi_\theta$. At the same $C_x$ range ($C_x < 0.1$), ensemble averages of spectra marginally exceed the theoretical (variance-preserving) shape at the high wavenumber end. Although this may affect the reliability of $\varepsilon$ at low $C_x$, it is less relevant for $\chi_\theta$ as the principal variance-containing band, that is,

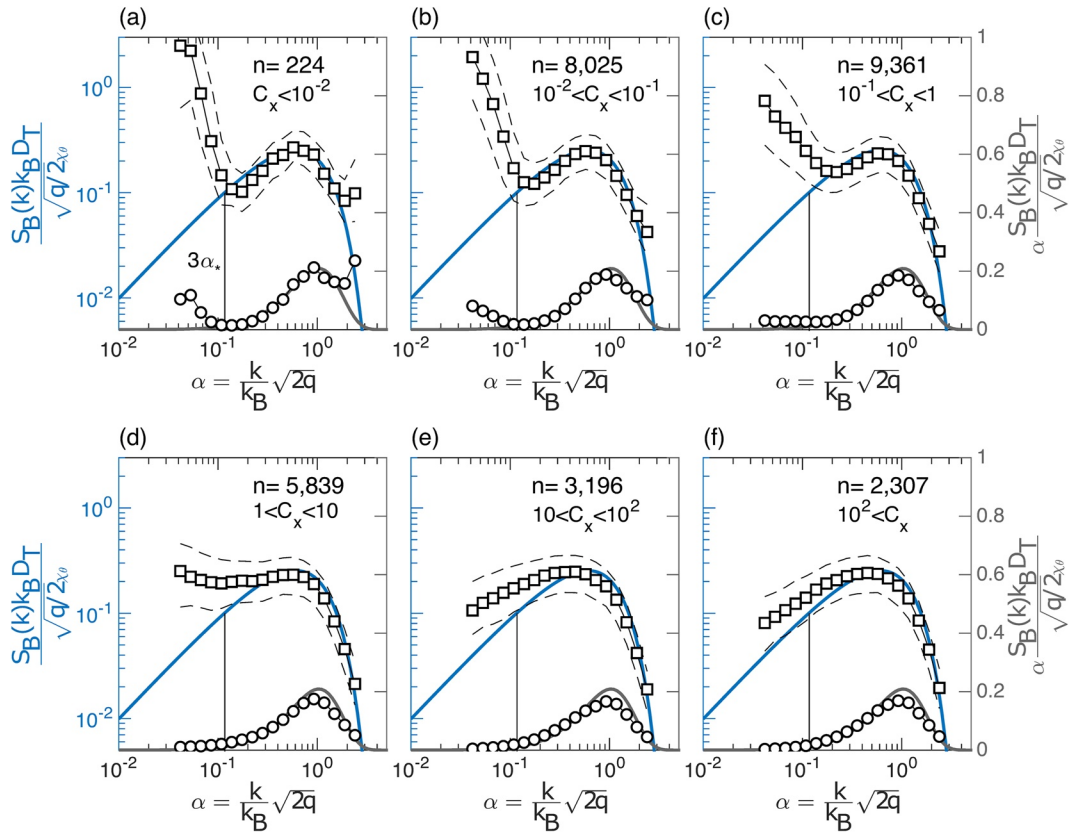


**Figure 5.** Spectral statistics following Dillon and Caldwell (1980). (a–f) The left *y*-axis corresponds to ensemble-median non-dimensional spectrum (squares) as a function of the non-dimensional wavenumber, $\alpha$, for Cox numbers ($C_x$) specified in the top right corner of each panel. This analysis considers spectra meeting the Ruddick et al. (2000) criteria from all missions (including both dives and climbs), with *n* indicating the number of evaluated spectra. Dashed envelopes represent 25th and 75th percentiles, respectively. The blue line is the non-dimensional Batchelor spectrum $\frac{S_B(k)k_B D_T}{\sqrt{(q/2)\chi_\theta}}$, where $q = 3.4$ is the universal spectral constant. The value $\alpha_* = 0.04\sqrt{\frac{D_T 2q}{\nu}} \approx 0.03$ (vertical black lines) corresponds to the non-dimensional form of the transitional wavenumber $k_*$. The right *y*-axis corresponds to the variance-preserving plot of ensemble-median non-dimensional spectrum (circles) presented in the left *y*-axis. The gray line is the variance-preserving non-dimensional Batchelor spectrum $\alpha \frac{S_B(k)k_B D_T}{\sqrt{(q/2)\chi_\theta}}$.

the spectra roll-off ($\alpha = 1$), remains adequately resolved. These results hold for separated dive and climb analyses (Figures S9 and S10 in Supporting Information S1). Figure 5 thus shows that our Batchelor spectra fitting procedure performs overall reliably, capturing the temperature gradient variance at the relevant wavenumber range.

### 4.3. Turbulence and Mixing: Comparison Between Interior and Coastal Slope

#### 4.3.1. Statistical and Vertical Distribution of Turbulent Quantities

We obtained estimations of turbulent dissipation ($\varepsilon$) and temperature variance smoothing rates ($\chi_\theta$) for all glider missions (Figure 6 and Table 2). The following examination concerns dives and climbs combined and considers procedure-compliant averages of turbulence estimates using the two fast thermistors mounted on the MicroRider. We discarded 47% of (averaged) estimates and refer to those remaining as samples. A comparison between dives and climbs is presented in the SI (Text S2, Figure S11 and Table S2 in Supporting Information S1) and demonstrates acceptable agreement.

For missions sampling the lake interior away from the slope (M1-M5; 21,334 samples), the statistics indicate overall weak-to-moderate turbulence (Figures 6a and 6d). The mle-mean for $\varepsilon$ and $\chi_\theta$ were 1.1 [0.96, 1.2] $\times 10^{-8}$ W kg$^{-1}$ and 1.8 [1.6, 2.0] $\times 10^{-8}$ °C$^2$ s$^{-1}$, respectively. Distributions of the interior-to-coast mission (M0; 1,859 samples) show similar characteristics, although high levels of turbulence were more frequent (Figures 6b and 6e). Dissipation rates for M0 were in the same range as in the interior (M1-M5), with a mle-mean

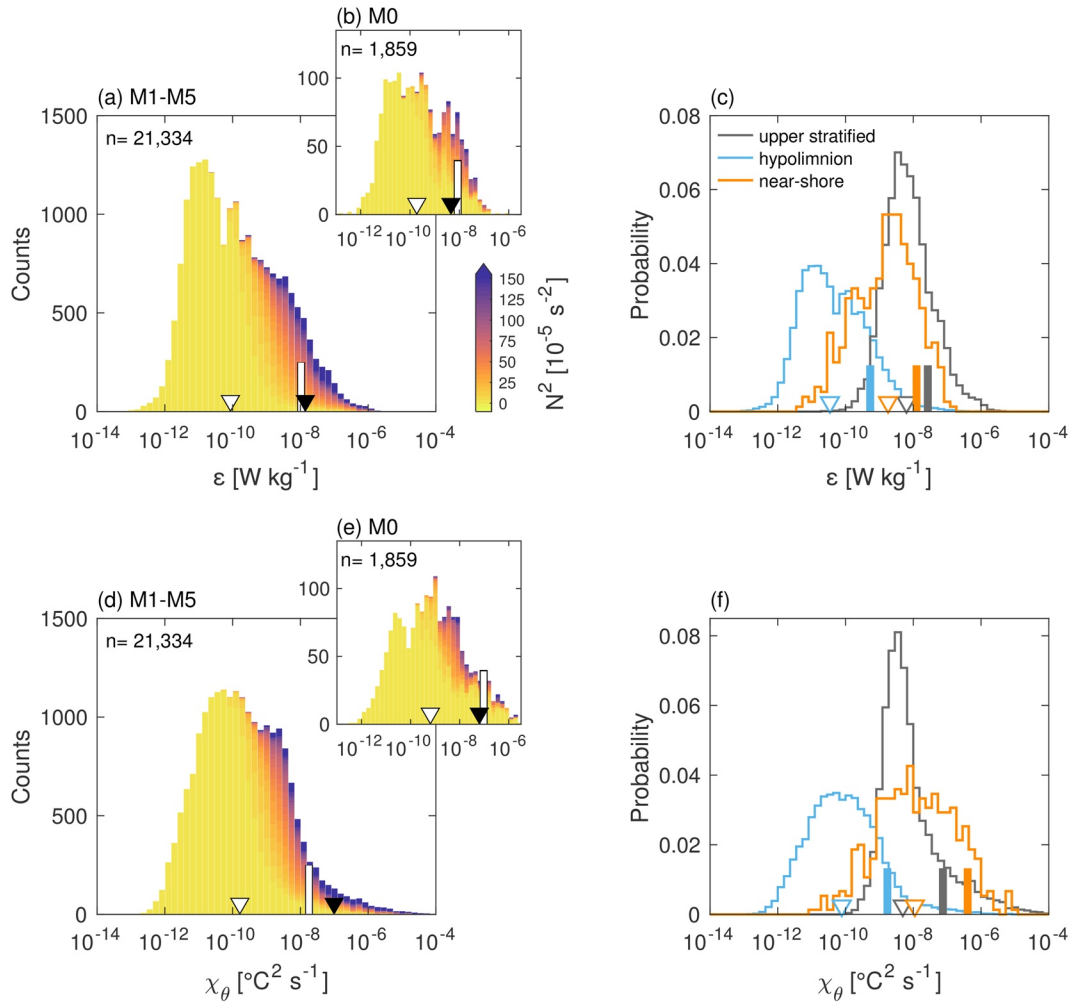


**Figure 6.** Statistics of measured turbulent characteristics. (a), (b) Histograms of turbulent dissipation, $\varepsilon$, grouped for lake interior (M1–M5) and interior-to-coast transition (M0), respectively, color-coded for water column stability ($N^2$). White vertical bars correspond to the mle-mean for a log-normal distribution (Baker & Gibson, 1987), while white and black triangles represent the median and arithmetic mean, respectively. (c) Probability distributions of $\varepsilon$ for different environments, namely: upper stratified (surface layer and thermocline combined; gray), hypolimnion (light blue) and near-shore (orange). Bars and triangles depict mle-mean and median, respectively. Upper stratified and hypolimnion sets consider all mission combined, whereas the near-shore set corresponds to estimates from mission M0 within 4 km from the shore. The stability threshold to separate upper stratified and hypolimnion was $N^2 = 3.0 \times 10^{-4}$ s$^{-2}$ (d, e, f) Analogous statistics as in (a, b, c) for the rate of temperature variance smoothing, $\chi_\theta$. The analysis considers only estimations that meet the Ruddick et al. (2000) criteria. Displayed data points were obtained by averaging the two estimates from the twin fast thermistors mounted on the MicroRider. Data segments with only one sample meeting the criteria were also considered.

of 0.86 [0.66, 1.1] $\times 10^{-8}$ W kg$^{-1}$. Temperature variance smoothing rates were, in contrast, one order of magnitude larger with a mle-mean of 9.5 [6.7, 13.0] $\times 10^{-8}$ °C$^2$ s$^{-1}$.

Different lake environments have distinct turbulence characteristics as a result of stratification (i.e., $N^2$-color code in Figures 6a and 6d) and or external forcing. Guided by transect results of temperature fluctuations gradients (Figures 3 and 4b), we compare turbulence statistics for the pelagic upper stratified region, the pelagic hypolimnion and the near-shore region (Figures 6c and 6f and Table 2 second row). The upper stratified region was more turbulent than the hypolimnion. Comparison of mle-means for $\varepsilon$ and $\chi_\theta$ resulted in differences of two and one order of magnitude, respectively. In the near-shore, $\varepsilon$ was comparable to the upper stratified (both $\sim 10^{-8}$ W kg$^{-1}$, with a factor 2 of difference). However, near-shore $\chi_\theta$ was one and two orders of magnitude higher than in the upper stratified region and hypolimnion, respectively. This feature signals a distinct mixing regime in the coastal area.

**Table 2**
*Statistical Summary of the Measured Turbulent Characteristics for Different Subsets of Interest*

| Parameter | Estimator | All | M1-M5 | M0 |
|---|---|---|---|---|
| $\varepsilon$ [$10^{-8}$ W kg$^{-1}$] | $\overline{X}_{\text{mle}}$ [LL, UL]$_{95\%}$ $\langle\sigma^2_{mle}\rangle$ | 1.0 [0.96, 1.1] ⟨8.7⟩ | 1.1 [0.96, 1.2] ⟨8.8⟩ | 0.86 [0.66, 1.1] ⟨7.3⟩ |
| | median [25th, 75th] | 0.0092 [0.0012, 0.12] | 0.0086 [0.0012, 0.11] | 0.019 [0.0026, 0.20] |
| | $\overline{x}$ ± std | 1.3 ± 46.0 | 1.4 ± 48.0 | 0.46 ± 2.4 |
| $\chi_\theta$ [$10^{-8}$ °C$^2$ s$^{-1}$] | $\overline{X}_{\text{mle}}$ [LL, UL]$_{95\%}$ $\langle\sigma^2_{mle}\rangle$ | 2.2 [2.0, 2.4] ⟨9.1⟩ | 1.8 [1.6, 2.0] ⟨8.9⟩ | 9.5 [6.7, 13.0] ⟨9.8⟩ |
| | median [25th, 75th] | 0.018 [0.0024, 0.17] | 0.016 [0.0023, 0.15] | 0.064 [0.0059, 0.61] |
| | $\overline{x}$ ± std | 9.6 ± 180.0 | 9.9 ± 190.0 | 6.3 ± 49.0 |
| | | Upper stratified | Hypolimnion | Near-shore |
| $\varepsilon$ [$10^{-8}$ W kg$^{-1}$] | $\overline{X}_{\text{mle}}$ [LL, UL]$_{95\%}$ $\langle\sigma^2_{mle}\rangle$ | 2.7 [2.5, 2.9] ⟨2.6⟩ | 0.054 [0.050, 0.057] ⟨4.9⟩ | 1.2 [0.90, 1.8] ⟨4.3⟩ |
| | median [25th, 75th] | 0.63 [0.24, 1.9] | 0.0035 [0.00085, 0.021] | 0.18 [0.031, 0.66] |
| | $\overline{x}$ ± std | 3.6 ± 14.0 | 0.73 ± 52.0 | 0.71 ± 1.5 |
| $\chi_\theta$ [$10^{-8}$ °C$^2$ s$^{-1}$] | $\overline{X}_{\text{mle}}$ [LL, UL]$_{95\%}$ $\langle\sigma^2_{mle}\rangle$ | 7.5 [6.8, 8.3] ⟨4.4⟩ | 0.2 [0.16, 0.18] ⟨5.9⟩ | 40 [24.0, 68.0] ⟨7.0⟩ |
| | median [25th, 75th] | 0.49 [0.22, 1.9] | 0.0077 [0.0016, 0.04] | 1.1 [0.17, 9.5] |
| | $\overline{x}$ ± std | 42.0 ± 390.0 | 1.0 ± 21.0 | 22.0 ± 95.0 |

*Note.* First block: Statistics of mission, considering the whole data set ("All"), interior (missions M1-M5) and interior-to-coast transition (mission M0). Second block: Statistics of different environments, namely, upper stratified (surface layer and thermocline combined), hypolimnion and near-shore (M0 within 4 km from the shore). Results are reported threefold, (i) mle-mean for a lognormal distribution, $\overline{X}_{\text{mle}}$, following Baker and Gibson (1987) accompanied by its 95% confidence interval and intermittency factor $\langle\sigma^2_{mle}\rangle$, (ii) median values with its respective 25th and 75th quantiles, and (iii) arithmetic mean $(\overline{x})$ ± standard deviation (std).

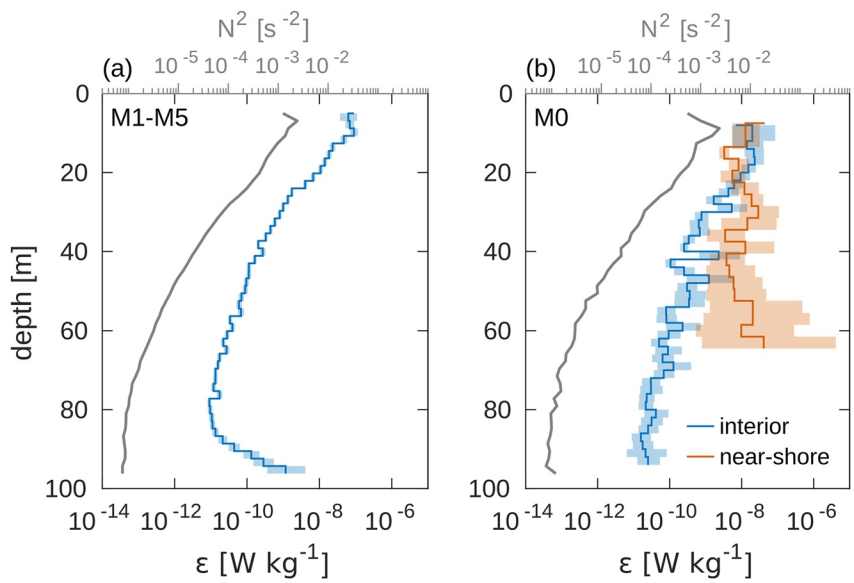


**Figure 7.** Vertical distribution of measured turbulent dissipation. (a) Interior (M1-M5) and (b) interior-to-coast transition (M0) separated for interior (blue) and near-shore (red). Profiles correspond to bin-averaged mle-means (lines) accompanied by their 95% confidence interval (transparent areas). Interior and near-shore profiles are presented using 2 and 3-m bins, respectively. Gray lines in (a) and (b) depict the water column stability ($N^2$) for each full sub-set. The interior dissipation profile shows an increase when approaching 100 m depth. We attribute this to glider flight maneuvers and enhanced turbulence near bottom slopes (see Text S2 in Supporting Information S1).

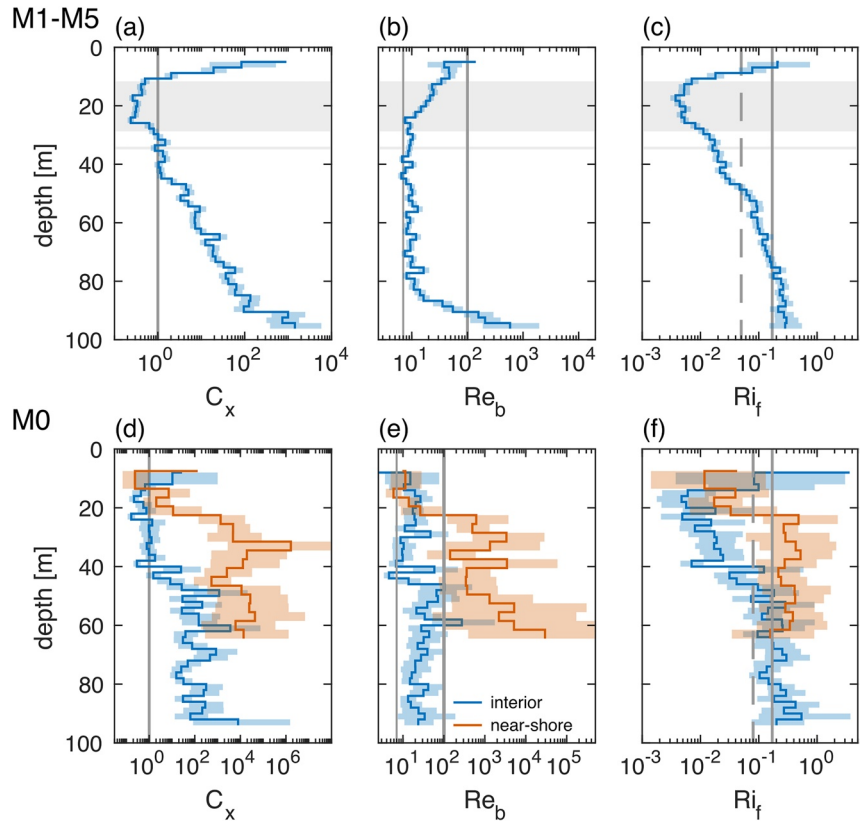


**Figure 8.** Average profiles of mixing quantities. (a)–(c) Lake interior (M1-M5) mle-mean profiles (blue lines) of $C_x$, $Re_b$ and $Ri_f$, respectively. Light blue areas in (a)–(c) represent the mle-mean 95% confidence interval. The gray vertical line in (a) is $C_x = K_T D_T^{-1} = 1$. Thin and thick gray vertical lines in (b) depict the lower and upper limits of the transitional regime ($7 < Re_b < 100$; Ivey et al., 2008). The continuous gray vertical line in (c) represents the canonical oceanic mixing efficiency $Ri_f = 0.17$ (Osborn, 1980). Regions of the interior water column exhibiting inhibited mixing ($C_x < 1$; i.e., $Ri_f$ is unreliable) are highlighted in light gray. (d)–(f) Analogous to (a)–(c) for mission M0 separating interior (blue) and near-shore (red) regions. Note that the $x$-axes are different between upper and lower panels. Dashed vertical lines in (c) and (f) show medians of $Ri_f$, satisfying $C_x > 1$ and $10 < Re_b < 1000$, in the interior ($Ri_f = 0.05$) and the interior-to-coast transition mission (M0; $Ri_f = 0.08$), respectively.

Vertical distributions of turbulence parameters (Figure 7 and Figure S12 in Supporting Information S1) show different responses to stratification in the interior and near-shore environments. The lake interior (Figure 7a and Figure S12a in Supporting Information S1) exhibited an overall decrease of $\varepsilon$ and $\chi_\theta$ with depth, and maximal $\varepsilon$ values were detected in the zone of sharper gradients (i.e., high $N^2$). This $N^2$-$\varepsilon$ dependence is further sustained by a positive linear relation in log-log space ($\log_{10}(\varepsilon/\varepsilon_{median}) = 0.99 \cdot \log_{10}\left(N^2/N^2_{median}\right) - 0.17$; $R^2 = 0.74$ and p-value <0.001). Measurements performed within 4 km of the shore during M0 (Figure 7b and Figure S12b in Supporting Information S1) show, in contrast, a clear enhancement of turbulence throughout the water column independent of stratification.

### 4.3.2. Turbulent Mixing

We present bin-averaged vertical profiles to analyze the mixing characteristics of the water column (Figure 8). In the interior, all three mixing parameters show maximal values in the upper stratified region (Figures 8a–8c), a zone influenced directly by wind forcing. Vertical profiles of $C_x$ and $Ri_f$ (Figures 8a and 8c, respectively) present minimum values around 20 m depth. The vertical profile of $Re_b$ (Figure 8b) shows that the water column lies almost entirely within the transitional regime ($7 < Re_b < 100$). Figure 8a–8c show inhibited mixing ($C_x < 1$, and thus $Ri_f \ll 0.1$) between 10 and 40 m depth, which comprises the thermocline region, despite exhibiting $7 < Re_b < 30$. This result is similar to that reported by Fernández Castro, Sepúlveda Steiner, et al. (2021) in deep Lake Zurich during stratified conditions.

The interior portion of M0 (Figure 8d–8f) shows similar characteristics to those in M1-M5 with inhibited mixing at the thermocline. Conversely, near-shore data shows a significant enhancement of turbulent mixing ($C_x$ of

$\mathcal{O}(10^{-3})$ and $Re_b > 100$), which also results in augmented mixing efficiency ($Ri_f > 0.17$). The more compact confidence intervals of mission M0 compared to those in the interior missions can be attributed to (a) the large difference in the number of samples per depth considered (five vs. one mission) and (b) intermittency and patchiness imposed by a more actively turbulent near-shore region. Enhanced turbulence and mixing above the sloping bottom may result from an interaction between flow and bathymetry. Altogether the interior shows weak turbulent mixing, which increases when approaching the coast.

### 4.4. Enhanced Dissipation Toward the Coastal Slope

Unlike the more uniform interior estimates of dissipation (M1-M5; Figure 7a), near shore M0 values show a clear enhancement of dissipation (Figures 7b and 12b) and mixing parameters (Figures 8d–8f). To better understand the differences between interior and near-shore regions, we present the transects of turbulent dissipation estimates (Figure 9a) and buoyancy flux (Figure 9b) for M0. The analysis reveals significant spatial variability and augmented values at the sloping topography ($\varepsilon$ of $\mathcal{O}(10^{-8})$ W kg$^{-1}$; $B \approx 7.4[4.8, 11.5] \times 10^{-9}$ W kg$^{-1}$, i.e., $\mathcal{O}(10^{-9})$). For the deep hypolimnion, dissipation estimates between interior and slope differ by up to three orders of magnitude. This enhancement of turbulence adjacent to the sloping topography consistently extends at depths above the reported height of bottom boundary layers in Lake Geneva during internal wave activity (~10 m; Bouffard & Lemmin, 2013a) and, in general, for medium (e.g., Wüest et al., 2000) and large lakes (Ravens et al., 2000; Troy et al., 2016).

### 4.5. External Forcing and Sources of TKE Variability

The wind is the main forcing of basin-scale circulation throughout the summer stratified conditions in Lake Geneva. Wind measurements during the field campaign (Figure 10a) showed moderate intensity, occasionally exceeding 5 m s$^{-1}$, and a predominant North-East direction (*La Bise*). Strong winds, consistently exceeding 5 m s$^{-1}$, were sporadic and associated with *Le Vent* events (South-West winds). Overall, the primary wind was *La Bise* and exhibited a daily cycle (Figure 10b).

We complemented our glider measurements with observations of horizontal current profiles at four different locations to obtain background information on basin-scale processes, which may result in spatial variability of TKE. Time series of current measurements from the four stations (Figure 2) are presented in Figure S13 in Supporting Information S1. Currents at the Buchillon coastal station (i.e., shallow waters) were more energetic than those measured in the interior, with dominant low-frequency periodicities (Figures 10b and 10c). In the lake interior, currents' rotary spectra (Figures 10b and 10c) were remarkably similar for the three open water monitored locations (ADCPs 1 to 3). Energized frequencies near the inertial frequency (period of ~16.6 hr for L. Geneva) in the clockwise component indicate the presence of Poincaré internal waves. This phenomenon has been identified to generate turbulent mixing in the lake interior (Bouffard et al., 2012). However, our results (Figures 8a–8c) do not support that mechanism of mixing generation, since mixing in the lake interior—where (near-inertial) Poincaré waves are dominant—was very week throughout our set of glider missions. At the Buchillon shore station, spectral energy levels exceeded those of the interior across the wavenumber spectrum, specifically at low frequencies. These peaks coincide with the expected bands of basin-scale internal Kelvin waves (~3.8 days; Bouffard & Lemmin, 2013a) and gyres.

## 5. Discussion

### 5.1. Glider Deployments and Their Sampling Potential in Lakes

This study reports and evaluates the spatiotemporal heterogeneity of turbulence in a large lake using an underwater glider. While mounting turbulence packages on gliders has now been established as a standard practice for oceanic measurements (e.g., Fer et al., 2014; Scheifele et al., 2018), such observations remain rare in lakes. Our results indicate that glider-based missions yield reliable turbulence measurements even in low turbulence and strongly stratified environments (Figures 5, 6, 7, and Figure S12 in Supporting Information S1), while collecting water quality parameters susceptible to turbulent transport (Figures S3-S8 in Supporting Information S1).

A significant advantage of glider missions is the possibility of collecting data during traditionally challenging weather conditions (e.g., strong winds, severe sea states; Carpenter et al., 2020; Schultze et al., 2020) or in inaccessible settings (e.g., below ice shelves; Friedrichs et al., 2022) over long periods. Under agitated conditions in medium-to-large lakes, gliders allow for the collection of measurements that would be otherwise impossible

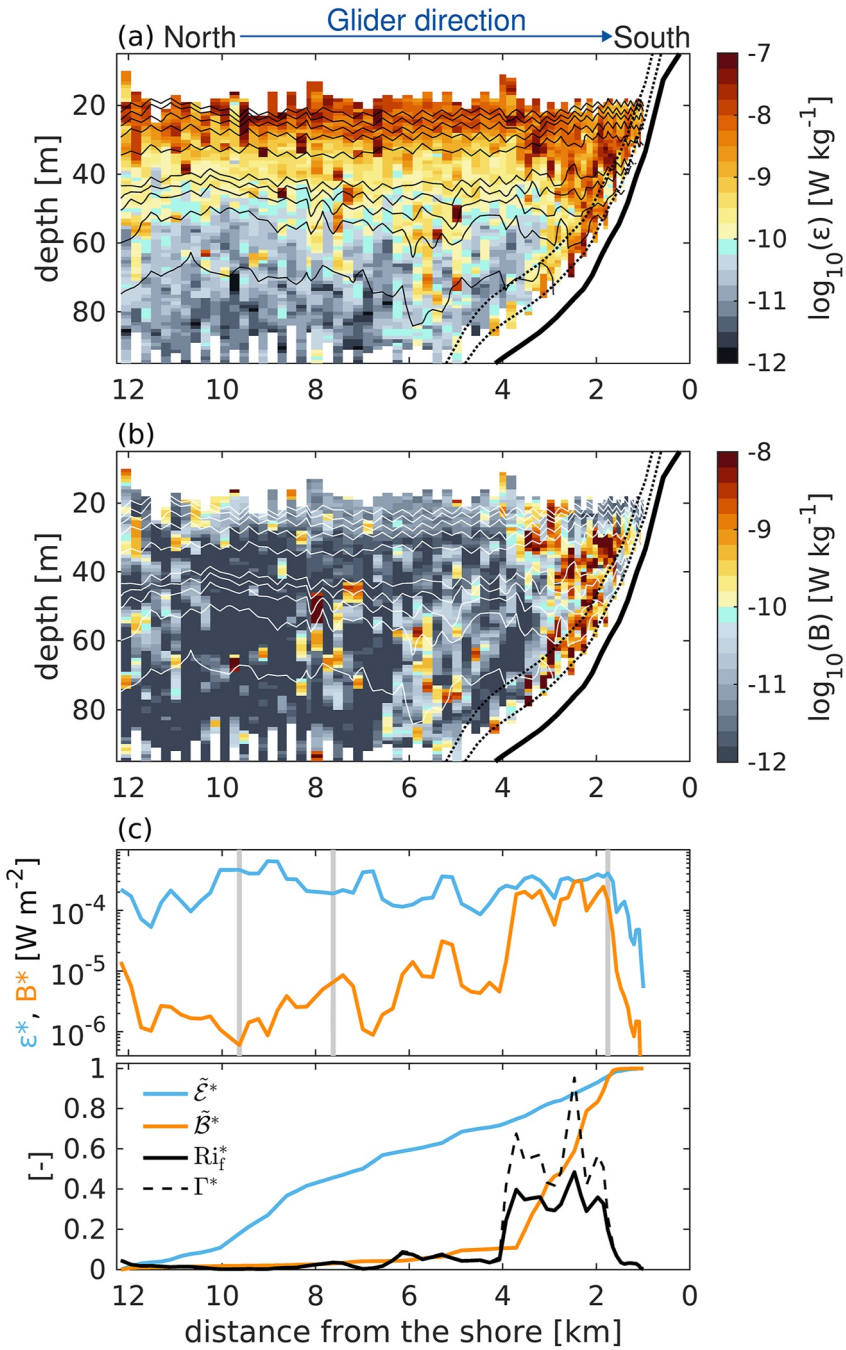


**Figure 9.** Cross-shore lateral variability. Data corresponding to mission M0, performed on 26 Jul 2018, starting at 10:50 a.m. local time. (a), (b) Glider-based turbulent dissipation ($\varepsilon$) and buoyancy flux (b), respectively. The thick black line represents the lake bottom, with dotted black lines depicting vertical displacements of the lake bed by 10 and 20 m, respectively. In (a) and (b), the horizontal resolution in the open waters (12-4 km from the shore) was about 205 m and increases from 200 to 50 m in the slope region (4-0 km from the shore). The collection of microstructure data was only possible due to the gentle slope of the mapped area. (c) Upper panel: Transect depth-integrated turbulent dissipation ($\varepsilon^* = \int \varepsilon(z)\rho(z)dz$; light blue line) and buoyancy flux ($B^* = \int B(z)\rho(z)dz$; orange line). Light gray vertical lines indicate manually-removed profiles exhibiting spikes in $B$ data. Lower panel: Normalized cross-shore cumulative integrals of turbulent dissipation $\left(\mathcal{E}^* = \int \varepsilon^* dx\right)$ and buoyancy flux $\left(\mathcal{B}^* = \int B^* dx\right)$, accompanied by cross-shore integrated estimates of the flux Richardson number ($Ri_f^* = \mathcal{B}^*/(\mathcal{B}^* + \mathcal{E}^*)$; black line) and the diapycnal flux coefficient ($\Gamma^* = \mathcal{B}^*/\mathcal{E}^*$; dashed black line).

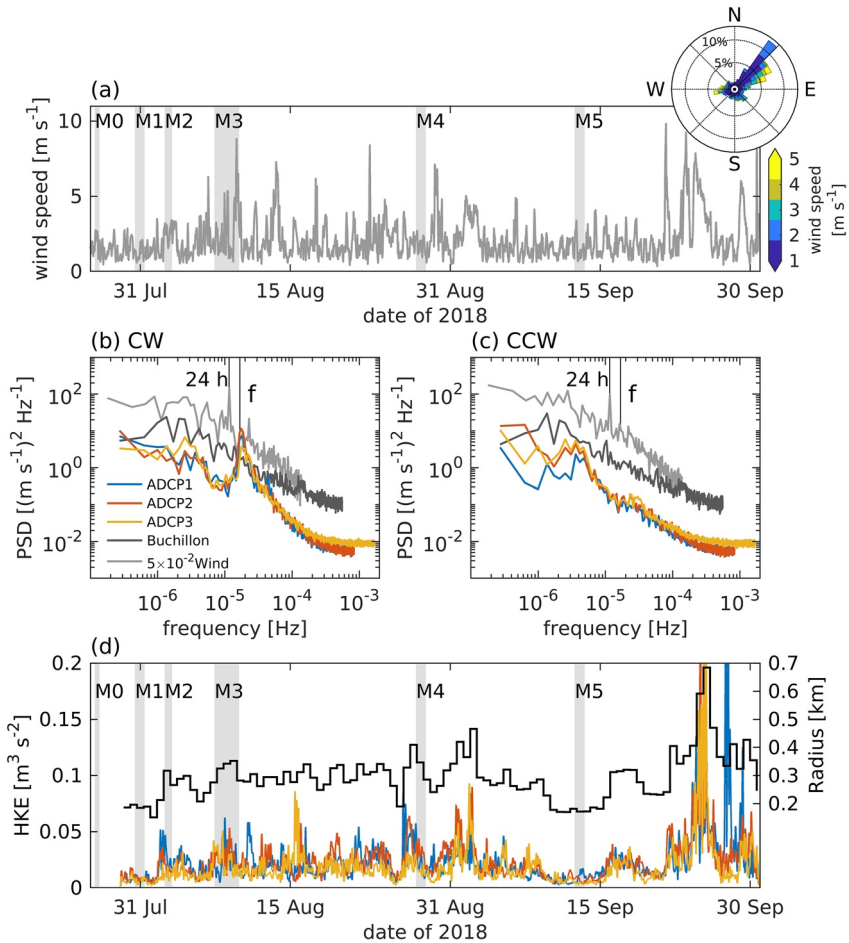


**Figure 10.** Wind data and current measurements analysis. (a) Wind speed time series and wind rose (direction) as measured at the Buchillon station. (b),(c) Median rotary power spectral density (PSD) for clockwise (CW; anti-cyclonic in northern hemisphere) and counter-clockwise (CCW; cyclonic) current components, respectively. The analysis considers the currents time series for each sampled bin throughout the water column. For convenience, the wind rotary PSD is presented scaled by a factor of $5 \times 10^{-2}$ to match the scale of currents PSDs. The inertial frequency is indicated by $f$ and corresponds to a period of 16.6 hr. (d) Left $y$-axis: Horizontal kinetic energy (HKE) of the inertial range of currents for ADCP1 to ADCP3. A bandpass filter around the inertial frequency of $[1, 5] \times 10^{-5}$ Hz was applied to the currents to perform the calculations. Right $y$-axis: Median radius of inertial currents (black line) obtained from the three HKE estimates, filtered with a 16 hr window average. Gray areas in (a) and (c) denote the periods of each glider mission.

to obtain through (small)ship-based operations. This challenge is particularly relevant in the case of turbulent quantities requiring tethered, free-falling profilers that risk severe damage (e.g., hitting bottom). Therefore, underwater gliders represent a qualitative breakthrough for data acquisition in these systems.

The relevance of the data collected with gliders depends on the spatial scale of interest. Our glider mission design, with immersions down to ∼100 m depth, seriously altered the possibility of investigating fine spatial variability at the interior thermocline, given the approximate 0.5 km horizontal distance between two consecutive dives. However, currents induced by the dominant basin-scale process, namely near-inertial waves (Figure 10), may generate heterogeneities in mixing and other quantities (e.g., Gregg et al., 1986; Marmorino et al., 1987) at length scales smaller than 0.5 km. Using the ADCP measurements, we estimated the HKE and a horizontal stirring length scale resulting from circulation at the dominant inertial frequency band (Figure 10d). This characteristic length was in the range of 0.2–0.4 km, suggesting that the spatial variability of thermocline diapycnal processes stemming from near-inertial wave horizontal stirring (e.g., Bouffard et al., 2012) was contained at scales smaller than those characterized by our glider missions.

In contrast to the quiet picture from the interior, Figures 9a and 9b suggest that glider deployments could be valuable for studying cross-shore turbulence patterns, particularly when approaching sloping boundaries. Safe glider navigation through steep bathymetry is the main complication to advance this knowledge. More agile underwater gliders (i.e., equipped with a shallow pump enabling faster vertical turns) and glider-mounted acoustics could help overcome technical barriers in spatial resolution and navigation close to the bottom.

### 5.2. Turbulence Estimates

Glider-based turbulence measurements have been mainly documented for energetic ocean environments (Fer et al., 2014; Schultze et al., 2017). The weak-to-moderate energetics of the strongly stratified Lake Geneva contrasts with the common use of gliders for turbulence estimates in oceanic conditions. This work reports a comprehensive method validation because a glider's along-path speed ($U \approx 0.35$ m s$^{-1}$) is two times faster than usual microstructure profiling speeds for lakes ($U \approx 0.15$ m s$^{-1}$; Kocsis et al., 1999), which may result in a limited capacity to resolve the smallest temperature fluctuations, critical to estimate TKE dissipation rates. We followed the approach of Dillon and Caldwell (1980), binned temperature microstructure spectra in different ranges of Cox number ($C_x$), and calculated their ensemble average (Figure 5). The analysis demonstrates that spectra meeting the Batchelor fitting conditions capture the variance and roll-off characteristics of the theoretical shape.

The encountered turbulence characteristics align well with those reported in the literature. Turbulence estimates in the interior (Figure 7a) presented a marked vertical structure with maximal values close to the surface ($\mathcal{O}(10^{-7})$ W kg$^{-1}$) that weakened with depth ($\mathcal{O}(10^{-11})$ W kg$^{-1}$). This result is consistent with the interior vertical profile in other deep stratified lakes (Fernández Castro, Sepúlveda Steiner, et al., 2021; Ravens et al., 2000). For our cross-shore transect (Figure 7b), the vertical decay of turbulent dissipation rates ranged between $10^{-10} - 10^{-8}$ W kg$^{-1}$ in the interior hypolimnion. The sloping near-shore region exhibited, in contrast, a more uniform profile ranging between $10^{-9}$ and $10^{-8}$ W kg$^{-1}$, which agrees with the average summer profile reported for Lake Geneva in a coastal location (Fernández Castro, Bouffard, et al., 2021).

At low $Re_b$ values (e.g., $Re_b < 10$ in Figures 8b and 8e), anisotropic turbulence is expected (Bluteau et al., 2011; Smyth & Moum, 2000a), such that turbulence estimates (and mixing coefficients) must be interpreted with caution. In another deep and strongly stratified lake exhibiting low $Re_b$, Fernández Castro, Sepúlveda Steiner, et al. (2021) reported comparable energy dissipation results from microstructure profiles and high-resolution ADCP measurements (through structure functions) processed using isotropic assumptions. The agreement between the two methods and consistency with previous observations in other systems was considered an argument for confidence in the data. In this work, we further rely upon the performed spectral shape validation (Figure 5), which confirms that spectral processing yields an adequate filter of low-quality data. While anisotropy may affect measurements in the deep interior, near-shore estimates above the slope seem unaffected (high $Re_b$ values; red line in Figure 8e).

The presented cross-shore data reveals a turbulent dissipation enhancement of one to two orders of magnitude in the near-shore slope with respect to the interior (Figure 7b). This general picture is in good agreement with seminal studies using vertical profile measurements to characterize turbulence in the different lake environments (MacIntyre et al., 1999; Wüest et al., 1996). We incorporate a more extensive amount of measurements and a highly resolved horizontal sampling (Figure 9a). Comparable spatially-distributed measurements in a near-shore region of Lake Geneva were performed with microstructure sensors mounted on a piloted submarine (Fer et al., 2002). Although their measurements were performed in winter, when stratification is weaker, our turbulent dissipation estimates near the slopes ($10^{-9} - 10^{-8}$ W kg$^{-1}$) agree with those reported by Fer et al. (2002), during windy conditions.

### 5.3. Mixing Characterization

There is a long-standing debate on the magnitude of mixing efficiency in natural waters, particularly whether it can be treated as a constant ($Ri_f = 0.17$ in the ocean; Osborn, 1980) or needs to be parameterized as a function of turbulence characteristics. The use of a constant value for $Ri_f$ is a standard practice in turbulence research, often due to data limitations and a large scatter of observational estimates. This approach has been further supported by the emerging concept of marginal instability (Smyth, 2020). However, there is mounting evidence that $Ri_f$ varies consistently as a function of a range of turbulent quantities and several studies propose various parameterizations (e.g., Bouffard & Boegman, 2013; Ijichi & Hibiya, 2018; Imberger & Ivey, 1991; Monismith et al., 2018). Our

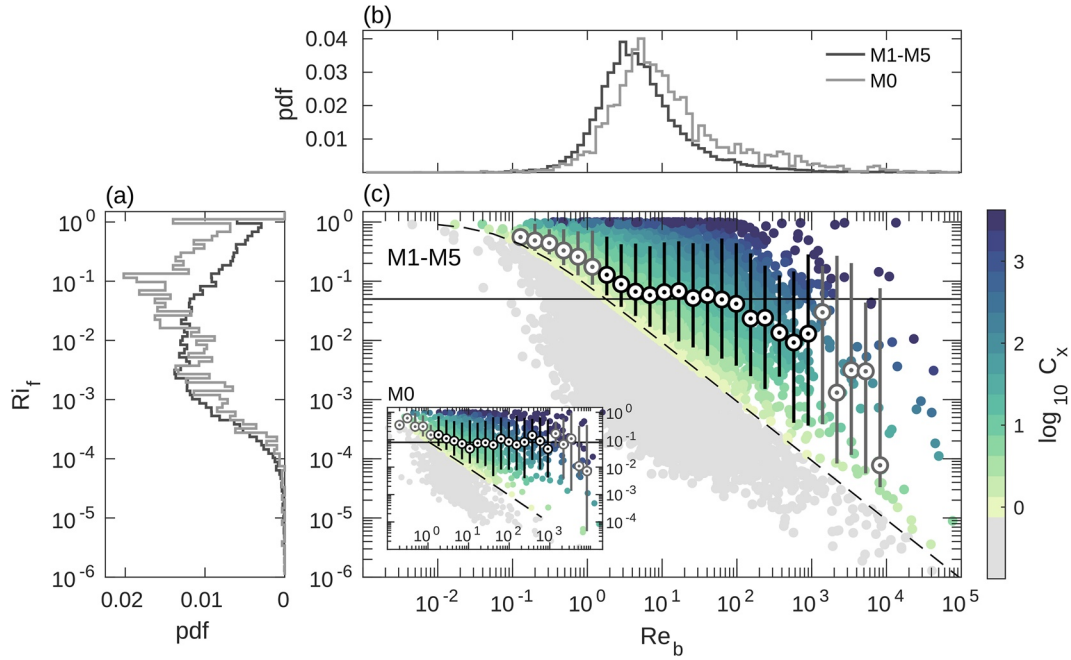


**Figure 11.** Mixing diagram. (a), (b) Probability density function (pdf) for the Richardson flux number ($Ri_f$) and the buoyancy Reynolds number ($Re_b$), respectively. (c) $Ri_f$ as a function of $Re_b$, color-coded for Cox numbers ($C_x$), considering the lake interior data set (M1-M5). Dotted white circles represent the median of $Ri_f$ in each bin for data points with $C_x > 1$. Error bars show 10th and 90th percentiles of the same subset. Black dotted-circles represent statistically well-conditioned intervals, with a reliable amount of data points, whereas those in gray are irrelevant or less reliable due to Re $\leq 1$ or few data points (Re $> 10^3$ intervals). The dashed black line is $Ri_f$ expressed as a function of $C_x$ and $Re_b$ (Equation 8) for $C_x = 1$. The horizontal black line corresponds to the median value of $Ri_f$ satisfying $C_x > 1$ and $10 < Re_b < 1{,}000$, $Ri_f = 0.05$. The inset plot in the left-inferior corner depicts the same analysis for the interior-to-coast transition data set (M0), with a median of $Ri_f = 0.08$.

glider-based turbulence dataset allows us to analyze the variability of $Ri_f$, and its dependency on turbulent parameters, such as $C_x$ and $Re_b$ (Figure 11) to help address this debate. The turbulent mixing data is available at the following repository: Sepúlveda Steiner et al. (2023b).

The interior thermocline region exhibited a combination of strong stratification and moderate TKE dissipation (Figure 7a). Strong background temperature gradients led to reduced Cox numbers ($C_x < 1$), suggesting that turbulent mixing was negligible (Figures 8a and 8c between 10 and 40 m), despite $7 < Re_b$ (i.e., transition to turbulence). This implies a very low mixing efficiency of $Ri_f \sim 0.01$, which is substantially below the canonical oceanic value in the lake interior ($Ri_f < Ri_f^{ocean} = 0.17$; Osborn, 1980). This result is in line with other studies of moderately energized lakes using microstructure methods (e.g., Etemad-Shahidi & Imberger, 2001; Fernández Castro, Sepúlveda Steiner, et al., 2021) and modeling (Umlauf & Lemmin, 2005) but differs from the strong thermocline mixing observed by Bouffard and Boegman (2013) in the shallow and energetic Lake Erie.

$Ri_f$ showed large variability (Figure 11) spanning more than five decades, with some marked dependency on $Re_b$. Binning interior data points with $C_x > 1$ only (i.e., turbulent temperature fluctuations overcome the background gradient) and averaging within the domain $10 < Re_b < 1{,}000$ yields a median and arithmetic mean $Ri_f$ values of 0.05 and $0.14 \pm 0.22$, respectively. Considering these values, the diapycnal flux coefficient, $\Gamma = \frac{Ri_f}{1-Ri_f}$, results in 0.05 and 0.16 for the median and arithmetic average. Monismith et al. (2018) found $Ri_f \approx 0.17$ ($\Gamma \approx 0.2$) below the thermocline for a compilation of oceanic datasets. Altogether, Figure 11 reveals that turbulent mixing in the interior of Lake Geneva was considerably less efficient during our sampling than in the ocean, raising concerns about the applicability of the Osborn diffusivity model in lakes. This firmly indicates that mixing efficiency characterization in deep, strongly stratified, and weakly energized lakes requires further research. Notwithstanding, Figure 11 clearly shows the dependency of $Ri_f$ on $C_x$ and $Re_b$, supporting the need for more elaborated parameterizations of mixing efficiency (e.g., Mashayek et al., 2021).

Unlike the lake interior, our observations revealed active and efficient mixing ($C_x > 1$, $Ri_f > 0.1$, $Re_b > 100$) in the coastal transition zone below 20 m depth. This shift in the mixing regime (possibly a result of different mechanisms generating turbulence) is clearly illustrated in Figure 9c, which shows that the buoyancy flux (i.e., density mixing) is enhanced by one order of magnitude within 4-km of the shoreline. While the role of boundary mixing in basin-scale energy budgets is well established in limnology (Gloor et al., 2000; Goudsmit et al., 1997) and oceanography (de Lavergne et al., 2016, 2017), its importance in lakes has been traditionally attributed to enhanced dissipation in coastal areas due to frictional boundary stresses (Goudsmit et al., 2002). The cross-shore transect is consistent with this view in that locally augmented dissipation is observed near the slope (Figure 9a); however, depth-integrated $\varepsilon$ remains almost constant due to the decreasing bottom depth (Figure 9c upper panel). In contrast, the depth-integrated buoyancy flux increases by two orders of magnitude, signaling a mixing efficiency enhancement. Cumulative integrals along the cross-shore transect (Figure 9c lower panel) show that $\approx 90\%$ of mixing (i.e., integrated buoyancy flux, $\mathcal{B}^*$)—and only 30% energy dissipation—occurs in the 4 km near-shore region, reaching average mixing efficiency values of $Ri_f = 0.2$ ($\Gamma = 0.3$). Compared to the bottom boundary layer of another (steeper) coastal location of Lake Geneva (Fernández Castro, Bouffard, et al., 2021), the near-shore mixing efficiency reported herein was larger by a factor of 2. Altogether, our results suggest that the relevance of boundary regions for the basin-scale mixing of lakes is underpinned by much more efficient mixing conditions in these regions compared to the lake interior. The question then is what possible driving mechanisms sustain such enhanced mixing.

### 5.4. Flow-Bathymetry Interactions

The following discusses the hydrodynamic processes that may support the enhanced turbulence and mixing obtained for mission M0 (Figure 9). Our limited observations at the mapped sloping embayment are further complemented by velocity field results from the 3D lake forecast model meteolakes.ch (Baracchini et al., 2020, further description and validation in Text S3 and Figure S14 in Supporting Information S1). The model results indicate a systematic development of rotating along-shore currents fluctuating between cyclonic (or counter-clockwise in the Northern hemisphere; Figure S15 in Supporting Information S1) and anti-cyclonic (Figure S16 in Supporting Information S1) types. This is consistent with observed internal wave circulation in other regions of the lake (internal Poincaré and Kelvin waves as observed in open waters, ADCPs 1–3, and at the Buchillon station, respectively). Given the presence of rotational currents, we do not consider here the traditional mechanisms of propagating cross-shore internal waves (e.g., Becherer & Umlauf, 2011; Lemckert et al., 2004) reaching the sloping boundaries and locally enhancing turbulence by shearing and wave-breaking (Lorke, 2007; Nakayama et al., 2020). We focus instead on rotating and/or along-shore currents interacting with sloping bathymetry, whose importance has been recently highlighted in oceanographic literature but is still overlooked in lake research.

For the period comprising mission M0, the model results confirm a large-scale cyclonic circulation in the near-shore region consistent with internal Kelvin waves (Figures S15a,b in Supporting Information S1). This cyclonic circulation was also found during other periods of our sampling campaign (see meteolakes.ch). Recent advancements in ocean research have identified centrifugal and symmetric instabilities, resulting from cyclonic current-bathymetry interactions, as an efficient mechanism for transferring kinetic rotational energy from geostrophic flows to submesoscales (Gula et al., 2016; Wenegrat & Thomas, 2020). The resulting unbalanced motions promote horizontal transport and cascade energy to small scales, generating turbulence. Furthermore, centrifugal instabilities have been reported to trigger vigorous turbulent mixing at slopes (Naveira Garabato et al., 2019). The occurrence of these instabilities is tied to the direction of the vertical component of Ertel's potential vorticity, $q_v$, by:

$$q_v = (\zeta + f)N^2 < 0 \tag{11}$$

where $\zeta = \frac{\partial v}{\partial x} - \frac{\partial u}{\partial y}$ is the vertical relative vorticity with $u$ and $v$ the east- and north-ward velocity component, respectively, and $f$ the inertial frequency. Centrifugal instabilities develop in the presence of cyclonic background circulation (e.g., a Kelvin wave) when the resulting vertical relative vorticity is negative, and its magnitude exceeds the Earth's rotational forcing. Vertical relative vorticity estimates from modeled velocities were negative in a band above the sloping topography (Figures S15c,d in Supporting Information S1), similar to that of the buoyancy flux enhancement (Figure 9b). Although the coarse resolution of the model does not allow us to

draw any robust conclusion, the analysis suggests that centrifugal instabilities are an interesting and unaccounted process to comprehend boundary mixing in lakes.

The model also predicts the contrary case, anti-cyclonic currents (Figure S16 in Supporting Information S1). Although we do not have measurements at the analyzed embayment during the development of such currents, these are frequent (see meteolakes.ch), particularly in periods where the Kelvin wave crest propagates in distant perimeters. Frictional interaction of anti-cyclonic currents with sloping bottoms, producing vigorous mixing, has been detected in the Baltic Sea in the case of near-inertial waves (Lappe & Umlauf, 2016). They highlighted the existence of a turbulent bottom boundary layer of a few meters in thickness and found diapycnal flux coefficients reaching values of 0.2 in some near-bottom regions, comparable to our results during mission M0 (Figure 9).

Flow interactions with irregular bathymetry may also account for enhanced dissipation at frictional boundaries (e.g., the headland West of the M0 transect in Figure 2). Along-shore tidal currents interacting with abrupt topography have been reported to generate eddies resulting from drag-induced flow separation (Pawlak et al., 2003). Such a mechanism can increase energy dissipation (MacKinnon et al., 2019) and buoyancy flux (Edwards et al., 2004) in sloping near-bottom regions.

As closing energy budgets in lakes remains elusive, further investigations of along-shore processes interacting with sloping bathymetry may reveal unaccounted transport and mixing processes key to expanding these budgets to the spatial extent. Combining a cross-shore array of high vertical resolution moorings resolving temperature (e.g., Van Haren, 2018; van Haren et al., 2021) and velocity fluctuations (Lorke et al., 2008) with repeated glider transects is needed for future exploration.

## 6. Conclusions

Our analyses of spatially-distributed physical quantities in Lake Geneva offer the following conclusions.

- We present a comprehensive study of underwater glider-based turbulence measurements in lakes. Moreover, we validate the use of such moving platforms for turbulent dissipation estimates using temperature microstructure in strongly stratified and weak-to-moderate energetic systems.
- Our results indicate that gliders are better suited for characterizing spatial variability when focusing on basin-scale processes with characteristic scales larger than the resolution enabled by two consecutive profiles (or yo's). However, despite the specific conditions during the sampling in Lake Geneva, we provide a compelling example of how they enable connecting large to small (turbulence) scales and vertical to horizontal dimensions.
- Despite the comparatively elevated turbulent dissipation, consistent with the level of wind forcing and resulting turbulent transitional regime in upper stratified waters, our study indicates inhibited turbulent mixing at the pelagic thermocline.
- We observed an increase in water column TKE dissipation near the lake's coastal slope. Furthermore, we report a substantial boost in buoyancy flux leading to enhanced mixing efficiency in this region. This result strengthens the role of boundary regions for the basin scale mixing.
- This study suggests finally the potential relevance of rotational circulation interacting with sloping boundaries with, for instance, submesoscale instabilities, a potentially critical mechanism to study in large lakes.

Much effort is still needed to unravel the spatial extent of energy budgets in lakes. This research provides a first step in that direction. Future research could combine the glider approach presented here with seasonal monitoring of turbulence microstructure and small-scale velocity field in bottom boundary layers (Fernández Castro, Bouffard, et al., 2021) to reveal temporal and lake-wide resolved energy pathways. Further understanding of boundary mixing in lakes is particularly relevant as this modifies the overturning circulation and the transport of dissolved compounds at the water-sediments interface.

## Appendix A: Statistics of Turbulent Quantities

When dealing with turbulence estimates or mixing coefficients, arithmetic means or median values do not include the impact of spatial patchiness and intermittent elevated values. For this reason, we use the maximum likelihood estimator (mle) of the expected value for a log-normal distribution (Baker & Gibson, 1987), which has been demonstrated to deal appropriately with turbulence data. A semi-formal definition of the mle-mean and its

intermittency factor is as follows. Let $X \sim \log\mathcal{N}(\mu, \sigma^2)$ be a random variable following a log-normal distribution and $Y = \ln(X)$ be the log-transformed random variable (i.e., following a normal distribution). Considering a sample set $\{y_1, \ldots, y_n\}$ of observed data of $Y$ with sample size $n$, the arithmetic mean is $\overline{y} = \frac{1}{n}\sum_i y_i$ and the arithmetic variance is $s'^2 = \frac{1}{n}\sum_i \left(\overline{y} - y_i\right)^2$. According to Baker and Gibson (1987), the minimum variance unbiased estimator of $\sigma^2$ is $s^2 = \frac{n}{n-1}s'^2$ and the mle of the expected value of $X$ is given by:

$$\overline{X}_{\text{mle}} = e^{\overline{y}+\frac{s^2}{2}} \tag{A1}$$

The intermittency factor is $\sigma^2_{\text{mle}} = s^2$ and corresponds to the unbiased variance in log-space (i.e., an ad-hoc estimate of statistical variability). To provide a measure of uncertainties, we calculate the mle 95% confidence intervals. These are obtained for the above-defined estimator (Equation A1) through a parametric bootstrap method using a t-student quantile estimation to ensure reliable confidence intervals also for small sample sizes.

## Data Availability Statement

Field measurements and results supporting the findings of this research are available online in different repositories. Glider (science bay and MicroRider), flight model and ADCP data are available at Sepúlveda Steiner et al. (2023a): https://doi.org/10.5281/zenodo.4796653. Estimated turbulence and mixing parameters data are available at the Eawag Research Data Institutional Collection (Sepúlveda Steiner et al., 2023b, https://doi.org/10.25678/0008FC). Meteorological data is available at https://www.datalakes-eawag.ch (Data Portal/Buchillon Field Station). Finally, Lake Geneva 3D model results are available at www.meteolakes.ch (Data Order/API).

**Acknowledgments**

We want to thank Hannah Chmiel, Theo Baracchini, Rafael Reiss, and Claudio Thomas Halaby for their assistance during fieldwork and Cordielyn Goodrich for remote surveillance of the glider during overnight missions. Anton Schleiss (LCH, EPFL) kindly allowed us to use his pool for ballasting purposes. The staff of Rockland Scientific provided timely feedback and troubleshooting during the field campaign. We are grateful to Lucas Merckelbach for guidance and technical support with the flight model and Ilker Fer and Andreas Lorke for their comments on an early version of the manuscript. Valuable feedback from Kenneth Larrieu on analyzing glider navigational data, Alberto Naveira Garabato on centrifugal instabilities, Cintia Ramón Casañas on numerical modeling, Jay Austin on rotary spectra and Louis Vuilleumier on statistics strengthened the manuscript's presentation and discussion. We acknowledge Theo Baracchini for leading the development of meteolakes.ch and James Runnalls for currently maintaining it. The authors would like to thank one anonymous reviewer, Jeff Carpenter and the Editor Lars Umlauf, for their very constructive feedback as the manuscript improved remarkably through the review process. This work was funded by the Swiss National Science Foundation Sinergia grant CRSII2_160726 (*A Flexible Underwater Distributed Robotic System for High-Resolution Sensing of Aquatic Ecosystems*). The ENAC Visiting Professor Program funded A.L.F's visit to EPFL during 2018. O.S.S. was partially supported in 2022 by an Eawag Academic Transition Grant (ATG). Open access funding provided by ETH-Bereich Forschungsanstalten.

## References

Adrian, R., O'Reilly, C. M., Zagarese, H., Baines, S. B., Hessen, D. O., Keller, W., et al. (2009). Lakes as sentinels of climate change. *Limnology & Oceanography*, *54*(6part2), 2283–2297. https://doi.org/10.4319/lo.2009.54.6_part_2.2283

Alexander, R., & Imberger, J. (2013). Phytoplankton patchiness in Winam Gulf, Lake Victoria: A study using principal component analysis of in situ fluorescent excitation spectra. *Freshwater Biology*, *58*(2), 275–291. https://doi.org/10.1111/fwb.12057

Antenucci, J. P., Imberger, J., & Saggio, A. (2000). Seasonal evolution of the basin-scale internal wave field in a large stratified lake. *Limnology & Oceanography*, *45*(7), 1621–1638. https://doi.org/10.4319/lo.2000.45.7.1621

Appt, J., Imberger, J., & Kobus, H. (2004). Basin-scale motion in stratified Upper Lake Constance. *Limnology & Oceanography*, *49*(4), 919–933. https://doi.org/10.4319/lo.2004.49.4.0919

Austin, J. (2012). Resolving a persistent offshore surface temperature maximum in Lake Superior using an autonomous underwater glider. *Aquatic Ecosystem Health and Management*, *15*(3), 316–321. https://doi.org/10.1080/14634988.2012.711212

Austin, J. (2013). The potential for autonomous underwater gliders in large lake research. *Journal of Great Lakes Research*, *39*(S1), 8–13. https://doi.org/10.1016/j.jglr.2013.01.004

Austin, J. (2019). Observations of radiatively driven convection in a deep lake. *Limnology & Oceanography*, *64*(5), 2152–2160. https://doi.org/10.1002/lno.11175

Baker, M. A., & Gibson, C. H. (1987). Sampling turbulence in the stratified ocean: Statistical consequences of strong intermittency. *Journal of Physical Oceanography*, *17*(10), 1817–1836. https://doi.org/10.1175/1520-0485(1987)017<1817:stitso>2.0.co;2

Baracchini, T., Wüest, A., & Bouffard, D. (2020). Meteolakes: An operational online three-dimensional forecasting platform for lake hydrodynamics. *Water Research*, *172*, 115529. https://doi.org/10.1016/j.watres.2020.115529

Batchelor, G. K. (1959). Small-scale variation of convected quantities like temperature in turbulent fluid Part 1. General discussion and the case of small conductivity. *Journal of Fluid Mechanics*, *5*(1), 113–133. https://doi.org/10.1017/S002211205900009X

Bauer, S. W., Graf, W. H., Mortimer, C. H., & Perrinjaquet, C. (1981). Inertial motion in Lake Geneva (Le Léman). *Archives for Meteorology, Geophysics, and Bioclimatology Series A*, *30*(3), 289–312. https://doi.org/10.1007/BF02257850

Becherer, J. K., & Umlauf, L. (2011). Boundary mixing in lakes: 1. Modeling the effect of shear-induced convection. *Journal of Geophysical Research*, *116*(C10), C10017. https://doi.org/10.1029/2011JC007119

Bluteau, C. E., Jones, N. L., & Ivey, G. N. (2011). Estimating turbulent kinetic energy dissipation using the inertial subrange method in environmental flows. *Limnology and Oceanography: Methods*, *9*(7), 302–321. https://doi.org/10.4319/lom.2011.9.302

Bohle-Carbonell, M. (1986). Currents in Lake Geneva. *Limnology & Oceanography*, *31*(6), 1255–1266. https://doi.org/10.4319/lo.1986.31.6.1255

Bouffard, D., & Boegman, L. (2013). A diapycnal diffusivity model for stratified environmental flows. *Dynamics of Atmospheres and Oceans*, *61–62*, 14–34. https://doi.org/10.1016/j.dynatmoce.2013.02.002

Bouffard, D., Boegman, L., & Rao, Y. R. (2012). Poincaré wave–induced mixing in a large lake. *Limnology & Oceanography*, *57*(4), 1201–1216. https://doi.org/10.4319/lo.2012.57.4.1201

Bouffard, D., & Lemmin, U. (2013a). Kelvin waves in Lake Geneva. *Journal of Great Lakes Research*, *39*(4), 637–645. https://doi.org/10.1016/j.jglr.2013.09.005

Bouffard, D., & Lemmin, U. (2013b). A new sensor platform for investigating turbulence in stratified coastal environments. *Journal of Atmospheric and Oceanic Technology*, *30*(8), 1789–1802. https://doi.org/10.1175/JTECH-D-12-00159.1

Carpenter, J. R., Rodrigues, A., Schultze, L. K. P., Merckelbach, L. M., Suzuki, N., Baschek, B., & Umlauf, L. (2020). Shear instability and turbulence within a submesoscale front following a storm. *Geophysical Research Letters*, *47*(23), e2020GL090365. https://doi.org/10.1029/2020GL090365

Csanady, G. T. (1975). Hydrodynamics of large lakes. *Annual Review of Fluid Mechanics*, *7*(1), 357–386. https://doi.org/10.1146/annurev.fl.07.010175.002041

Davis, R. E., Eriksen, C. C., & Jones, C. (2002). Autonomous buoyancy-driven underwater gliders. In G. Griffiths (Ed.), *Technology and applications of autonomous underwater vehicles* (pp. 37–58). Taylor & Francis. https://doi.org/10.1201/9780203522301.ch3

De Lavergne, C., Madec, G., Capet, X., Maze, G., & Roquet, F. (2016). Getting to the bottom of the ocean. *Nature Geoscience*, *9*(12), 857–858. https://doi.org/10.1038/ngeo2850

De Lavergne, C., Madec, G., Roquet, F., Holmes, R. M., & Mcdougall, T. J. (2017). Abyssal ocean overturning shaped by seafloor distribution. *Nature*, *551*(7679), 181–186. https://doi.org/10.1038/nature24472

Dillon, T. M., & Caldwell, D. R. (1980). The Batchelor spectrum and dissipation in the upper ocean. *Journal of Geophysical Research*, *85*(C4), 1910–1916. https://doi.org/10.1029/JC085iC04p01910

Edwards, K. A., MacCready, P., Moum, J. N., Pawlak, G., Klymak, J. M., & Perlin, A. (2004). Form drag and mixing due to tidal flow past a sharp point. *Journal of Physical Oceanography*, *34*(6), 1297–1312. https://doi.org/10.1175/1520-0485(2004)034<1297:fdamdt>2.0.co;2;2

Etemad-Shahidi, A., & Imberger, J. (2001). Anatomy of turbulence in thermally stratified lakes. *Limnology & Oceanography*, *46*(5), 1158–1170. https://doi.org/10.4319/lo.2001.46.5.1158

Fer, I., Lemmin, U., & Thorpe, S. A. (2002). Observations of mixing near the sides of a deep lake in winter. *Limnology & Oceanography*, *47*(2), 535–544. https://doi.org/10.4319/lo.2002.47.2.0535

Fer, I., Peterson, A. K., & Ullgren, J. E. (2014). Microstructure measurements from an underwater glider in the turbulent Faroe Bank Channel overflow. *Journal of Atmospheric and Oceanic Technology*, *31*(5), 1128–1150. https://doi.org/10.1175/JTECH-D-13-00221.1

Fernández Castro, B., Bouffard, D., Troy, C., Ulloa, H. N., Piccolroaz, S., Sepúlveda Steiner, O., et al. (2021). Seasonality modulates wind-driven mixing pathways in a large lake. *Communications Earth & Environment*, *2*(1), 215. https://doi.org/10.1038/s43247-021-00288-3

Fernández Castro, B., Sepúlveda Steiner, O., Knapp, D., Posch, T., Bouffard, D., & Wüest, A. (2021). Inhibited vertical mixing and seasonal persistence of a thin cyanobacterial layer in a stratified lake. *Aquatic Sciences*, *83*(2), 38. https://doi.org/10.1007/s00027-021-00785-9

Forrest, A. L., Laval, B. E., Pieters, R., & Lim, D. S. S. (2008). Convectively driven transport in temperate lakes. *Limnology & Oceanography*, *53*(5), 2321–2332. https://doi.org/10.4319/lo.2008.53.5_part_2.2321

Friedrichs, D. M., McInerney, J. B., Oldroyd, H. J., Lee, W. S., Yun, S., Yoon, S.-T., et al. (2022). Observations of submesoscale eddy-driven heat transport at an ice shelf calving front. *Communications Earth & Environment*, *3*(1), 140. https://doi.org/10.1038/s43247-022-00460-3

Gargett, A. E., Osborn, T. R., & Nasmyth, P. W. (1984). Local isotropy and the decay of turbulence in a stratified fluid. *Journal of Fluid Mechanics*, *144*, 231–280. https://doi.org/10.1017/S0022112084001592

Gibson, C. H. (1980). Fossil temperature, salinity, and vorticity turbulence in the ocean. In J. C. Nihoul (Ed.), *Marine turbulence proceedings of the 11th International Liege colloquium on ocean hydrodynamics*, *Elsevier oceanography series* (Vol. 28, pp. 221–257). Elsevier/North-Holland Inc. https://doi.org/10.1016/S0422-9894(08)71223-6

Gloor, M., Wüest, A., & Imboden, D. M. (2000). Dynamics of mixed bottom boundary layers and its implications for diapycnal transport in a stratified, natural water basin. *Journal of Geophysical Research*, *105*(C4), 8629–8646. https://doi.org/10.1029/1999JC900303

Goudsmit, G.-H., Burchard, H., Peeters, F., & Wüest, A. (2002). Application of k-$\epsilon$ turbulence models to enclosed basins: The role of internal seiches. *Journal of Geophysical Research*, *107*(C12), 3230–3231. https://doi.org/10.1029/2001JC000954

Goudsmit, G.-H., Peeters, F., Gloor, M., & Wüest, A. (1997). Boundary versus internal diapycnal mixing in stratified natural waters. *Journal of Geophysical Research*, *102*(C13), 27903–27914. https://doi.org/10.1029/97JC01861

Gregg, M. C. (1977). Variations in the intensity of small-scale mixing in the main thermocline. *Journal of Physical Oceanography*, *7*(3), 436–454. https://doi.org/10.1175/1520-0485(1977)007<0436:vitios>2.0.co;2;2

Gregg, M. C., D'Asaro, E. A., Shay, T. J., & Larson, N. (1986). Observations of persistent mixing and near-inertial internal waves. *Journal of Physical Oceanography*, *16*(5), 856–885. https://doi.org/10.1175/1520-0485(1986)016<0856:oopman>2.0.co;2

Gula, J., Molemaker, M. J., & McWilliams, J. C. (2016). Topographic generation of submesoscale centrifugal instability and energy dissipation. *Nature Communications*, *7*(1), 12811. https://doi.org/10.1038/ncomms12811

Ijichi, T., & Hibiya, T. (2018). Observed variations in turbulent mixing efficiency in the deep ocean. *Journal of Physical Oceanography*, *48*(8), 1815–1830. https://doi.org/10.1175/JPO-D-17-0275.1

Imberger, J. (1998). Flux paths in a stratified lake: A review. In J. Imberger (Ed.), *Physical processes in lakes and oceans* (pp. 1–17). American Geophysical Union (AGU). https://doi.org/10.1029/CE054p0001

Imberger, J., & Ivey, G. N. (1991). On the nature of turbulence in a stratified fluid. Part II: Application to lakes. *Journal of Physical Oceanography*, *21*(5), 659–680. https://doi.org/10.1175/1520-0485(1991)021<0659:otnoti>2.0.co;2;2

Ishikawa, K., Kumagai, M., Vincent, W. F., Tsujimura, S., & Nakahara, H. (2002). Transport and accumulation of bloom-forming cyanobacteria in a large, mid-latitude lake: The gyre-Microcystis hypothesis. *Limnology*, *3*(2), 87–96. https://doi.org/10.1007/s102010200010

Ivey, G. N., & Imberger, J. (1991). On the nature of turbulence in a stratified fluid. Part I: The energetics of mixing. *Journal of Physical Oceanography*, *21*(5), 650–658. https://doi.org/10.1175/1520-0485(1991)021<0650:otnoti>2.0.co;2

Ivey, G. N., Winters, K. B., & Koseff, J. R. (2008). Density stratification, turbulence, but how much mixing? *Annual Review of Fluid Mechanics*, *40*(1), 169–184. https://doi.org/10.1146/annurev.fluid.39.050905.110314

Jassby, A., & Powell, T. (1975). Vertical patterns of eddy diffusion during stratification in Castle Lake, California. *Limnology & Oceanography*, *20*(4), 530–543. https://doi.org/10.4319/lo.1975.20.4.0530

Kocsis, O., Prandke, H., Stips, A., Simon, A., & Wüest, A. (1999). Comparison of dissipation of turbulent kinetic energy determined from shear and temperature microstructure. *Journal of Marine Systems*, *21*(1–4), 67–84. https://doi.org/10.1016/S0924-7963(99)00006-8

Lappe, C., & Umlauf, L. (2016). Efficient boundary mixing due to near-inertial waves in a nontidal basin: Observations from the Baltic Sea. *Journal of Geophysical Research: Oceans*, *121*(11), 8287–8304. https://doi.org/10.1002/2016JC011985

Laval, B., Bird, J. S., & Helland, P. D. (2000). An autonomous underwater vehicle for the study of small lakes. *Journal of Atmospheric and Oceanic Technology*, *17*(1), 69–76. https://doi.org/10.1175/1520-0426(2000)017<0069:aauvft>2.0.co;2;2

Laval, B., Imberger, J., & Findikakis, A. N. (2005). Dynamics of a large tropical lake: Lake Maracaibo. *Aquatic Sciences*, *67*(3), 337–349. https://doi.org/10.1007/s00027-005-0778-1

Lemckert, C., Antenucci, J., Saggio, A., & Imberger, J. (2004). Physical properties of turbulent benthic boundary layers generated by internal waves. *Journal of Hydraulic Engineering*, *130*(1), 58–69. https://doi.org/10.1061/(asce)0733-9429(2004)130:1(58)

Lemmin, U., & D'Adamo, N. (1996). Summertime winds and direct cyclonic circulation: Observations from Lake Geneva. *Annales Geophysicae*, *14*(11), 1207–1220. https://doi.org/10.1007/s00585-996-1207-z

Lemmin, U., Mortimer, C. H., & Bäuerle, E. (2005). Internal seiche dynamics in Lake Geneva. *Limnology & Oceanography*, *50*(1), 207–216. https://doi.org/10.4319/lo.2005.50.1.0207

Lorke, A. (2007). Boundary mixing in the thermocline of a large lake. *Journal of Geophysical Research*, *112*(C9), C09019. https://doi.org/10.1029/2006JC004008

Lorke, A., Umlauf, L., & Mohrholz, V. (2008). Stratification and mixing on sloping boundaries. *Geophysical Research Letters*, *35*(L14610), L14610. https://doi.org/10.1029/2008GL034607

Lucas, N. S., Grant, A. L. M., Rippeth, T. P., Polton, J. A., Palmer, M. R., Brannigan, L., & Belcher, S. E. (2019). Evolution of oceanic near-surface stratification in response to an autumn storm. *Journal of Physical Oceanography*, *49*(11), 2961–2978. https://doi.org/10.1175/JPO-D-19-0007.1

Luketina, D. A., & Imberger, J. (2001). Determining turbulent kinetic energy dissipation from Batchelor curve fitting. *Journal of Atmospheric and Oceanic Technology*, *18*(1), 100–113. https://doi.org/10.1175/1520-0426(2001)018<0100:dtkedf>2.0.co;2

MacIntyre, S., Flynn, K. M., Jellison, R., & Romero, J. R. (1999). Boundary mixing and nutrient fluxes in Mono Lake, California. *Limnology & Oceanography*, *44*(3), 512–529. https://doi.org/10.4319/lo.1999.44.3.0512

MacIntyre, S., Romero, J. R., & Kling, G. W. (2002). Spatial-temporal variability in surface layer deepening and lateral advection in an embayment of Lake Victoria, East Africa. *Limnology & Oceanography*, *47*(3), 656–671. https://doi.org/10.4319/lo.2002.47.3.0656

MacIntyre, S., Romero, J. R., Silsbe, G. M., & Emery, B. M. (2014). Stratification and horizontal exchange in Lake Victoria, East Africa. *Limnology & Oceanography*, *59*(6), 1805–1838. https://doi.org/10.4319/lo.2014.59.6.1805

MacKinnon, J. A., Alford, M. H., Voet, G., Zeiden, K. L., Shaun Johnston, T. M., Siegelman, M., et al. (2019). Eddy wake generation from broadband currents near Palau. *Journal of Geophysical Research: Oceans*, *124*(7), 4891–4903. https://doi.org/10.1029/2019JC014945

Marmorino, G. O., Rosenblum, L. J., & Trump, C. L. (1987). Fine-scale temperature variability: The influence of near-inertial waves. *Journal of Geophysical Research*, *92*(C12), 13049. https://doi.org/10.1029/JC092iC12p13049

Mashayek, A., Caulfield, C., & Alford, M. (2021). Goldilocks mixing in oceanic shear-induced turbulent overturns. *Journal of Fluid Mechanics*, *928*, A1. https://doi.org/10.1017/jfm.2021.740

McDougall, T. J., & Barker, P. (2011). Getting started with TEOS-10 and the Gibbs Seawater (GSW) oceanographic toolbox. *SCOR/IAPSO WG*, *127*, 1–28.

McInerney, J. B., Forrest, A. L., Schladow, S. G., & Largier, J. L. (2019). How to fly an autonomous underwater glider to measure an internal wave. In *Oceans 2019 MTS/IEEE SEATTLE* (pp. 1–8). https://doi.org/10.23919/OCEANS40490.2019.8962407

Merckelbach, L., Berger, A., Krahmann, G., Dengler, M., & Carpenter, J. R. (2019). A dynamic flight model for Slocum gliders and implications for turbulence microstructure measurements. *Journal of Atmospheric and Oceanic Technology*, *36*(2), 281–296. https://doi.org/10.1175/JTECH-D-18-0168.1

Michalski, J., & Lemmin, U. (1995). Dynamics of vertical mixing in the hypolimnion of a deep lake: Lake Geneva. *Limnology & Oceanography*, *40*(4), 809–816. https://doi.org/10.4319/lo.1995.40.4.0809

Monismith, S. G., Koseff, J. R., & White, B. L. (2018). Mixing efficiency in the presence of stratification: When is it constant? *Geophysical Research Letters*, *45*(11), 5627–5634. https://doi.org/10.1029/2018GL077229

Nakayama, K., Sato, T., Tani, K., Boegman, L., Fujita, I., & Shintani, T. (2020). Breaking of internal Kelvin waves shoaling on a slope. *Journal of Geophysical Research: Oceans*, *125*(10), e2020JC016120. https://doi.org/10.1029/2020JC016120

Naveira Garabato, A. C., Frajka-Williams, E. E., Spingys, C. P., Legg, S., Polzin, K. L., Forryan, A., et al. (2019). Rapid mixing and exchange of deep-ocean waters in an abyssal boundary current. *Proceedings of the National Academy of Sciences*, *116*(27), 13233–13238. https://doi.org/10.1073/pnas.1904087116

Osborn, T. R. (1980). Estimates of the local rate of vertical diffusion from dissipation measurements. *Journal of Physical Oceanography*, *10*(1), 83–89. https://doi.org/10.1175/1520-0485(1980)010<0083:eotlro>2.0.co;2

Osborn, T. R., & Cox, C. S. (1972). Oceanic fine structure. *Geophysical Fluid Dynamics*, *3*(1), 321–345. https://doi.org/10.1080/03091927208236085

Osborn, T. R., & Lueck, R. G. (1985). Turbulence measurements with a submarine. *Journal of Physical Oceanography*, *15*(11), 1502–1520. https://doi.org/10.1175/1520-0485(1985)015<1502:tmwas>2.0.co;2

Pawlak, G., MacCready, P., Edwards, K. A., & McCabe, R. (2003). Observations on the evolution of tidal vorticity at a stratified deep water headland. *Geophysical Research Letters*, *30*(24), 2234. https://doi.org/10.1029/2003GL018092

Peterson, A. K., & Fer, I. (2014). Dissipation measurements using temperature microstructure from an underwater glider. *Methods in Oceanography*, *10*, 44–69. https://doi.org/10.1016/j.mio.2014.05.002

Ravens, T. M., Kocsis, O., Wüest, A., & Granin, N. (2000). Small-scale turbulence and vertical mixing in Lake Baikal. *Limnology & Oceanography*, *45*(1), 159–173. https://doi.org/10.4319/lo.2000.45.1.0159

Reiss, R. S., Lemmin, U., Cimatoribus, A. A., & Barry, D. A. (2020). Wintertime coastal upwelling in Lake Geneva: An efficient transport process for deepwater renewal in a large, deep lake. *Journal of Geophysical Research: Oceans*, *125*(8), e2020JC016095. https://doi.org/10.1029/2020JC016095

Roberts, D. C., Egan, G. C., Forrest, A. L., Largier, J. L., Bombardelli, F. A., Laval, B. E., et al. (2021). The setup and relaxation of spring upwelling in a deep, rotationally influenced lake. *Limnology & Oceanography*, *66*(4), 1168–1189. https://doi.org/10.1002/lno.11673

Ruddick, B., Anis, A., & Thompson, K. (2000). Maximum likelihood spectral fitting: The Batchelor spectrum. *Journal of Atmospheric and Oceanic Technology*, *17*(11), 1541–1555. https://doi.org/10.1175/1520-0426(2000)017<1541:mlsftb>2.0.co;2

Rudnick, D. L. (2016). Ocean research enabled by underwater gliders. *Annual Review of Marine Science*, *8*(1), 519–541. https://doi.org/10.1146/annurev-marine-122414-033913

Saggio, A., & Imberger, J. (2001). Mixing and turbulent fluxes in the metalimnion of a stratified lake. *Limnology & Oceanography*, *46*(2), 392–409. https://doi.org/10.4319/lo.2001.46.2.0392

Sahoo, G. B., Forrest, A. L., Schladow, S. G., Reuter, J. E., Coats, R., & Dettinger, M. (2016). Climate change impacts on lake thermal dynamics and ecosystem vulnerabilities. *Limnology & Oceanography*, *61*(2), 496–507. https://doi.org/10.1002/lno.10228

Scheifele, B., Waterman, S., & Carpenter, J. R. (2021). Turbulence and mixing in the Arctic Ocean's Amundsen Gulf. *Journal of Physical Oceanography*, *51*(1), 169–186. https://doi.org/10.1175/JPO-D-20-0057.1

Scheifele, B., Waterman, S., Merckelbach, L., & Carpenter, J. R. (2018). Measuring the dissipation rate of turbulent kinetic energy in strongly stratified, low-energy environments: A case study from the Arctic ocean. *Journal of Geophysical Research: Oceans*, *123*(8), 5459–5480. https://doi.org/10.1029/2017JC013731

Schladow, S. G., Pálmarsson, S. Ó., Steissberg, T. E., Hook, S. J., & Prata, F. E. (2004). An extraordinary upwelling event in a deep thermally stratified lake. *Geophysical Research Letters*, *31*(15), L15504. https://doi.org/10.1029/2004GL020392

Schultze, L. K. P., Merckelbach, L. M., & Carpenter, J. R. (2017). Turbulence and mixing in a shallow shelf sea from underwater gliders. *Journal of Geophysical Research: Oceans*, *122*(11), 9092–9109. https://doi.org/10.1002/2017JC012872

Schultze, L. K. P., Merckelbach, L. M., & Carpenter, J. R. (2020). Storm-induced turbulence alters shelf sea vertical fluxes. *Limnology and Oceanography Letters*, *5*(3), 264–270. https://doi.org/10.1002/lol2.10139

Schwefel, R., Gaudard, A., Wüest, A., & Bouffard, D. (2016). Effects of climate change on deepwater oxygen and winter mixing in a deep lake (Lake Geneva): Comparing observational findings and modeling. *Water Resources Research*, *52*(11), 8811–8826. https://doi.org/10.1002/2016WR019194

Sepúlveda Steiner, O., Forrest, A. L., McInerney, J. B. T., Fernández Castro, B., Lavanchy, S., Wüest, A., & Bouffard, D. (2023a). Lake Geneva 2018 spatial variability dataset: Underwater glider, MicroRider and ADCPs [dataset]. Zenodo. https://doi.org/10.5281/zenodo.4796653

Sepúlveda Steiner, O., Forrest, A. L., McInerney, J. B. T., Fernández Castro, B., Lavanchy, S., Wüest, A., & Bouffard, D. (2023b). Lake Geneva 2018 underwater glider-based turbulent mixing data [Dataset]. Swiss Federal Institute of Aquatic Science and Technology. https://doi.org/10.25678/0008FC

Shimizu, K., Imberger, J., & Kumagai, M. (2007). Horizontal structure and excitation of primary motions in a strongly stratified lake. *Limnology & Oceanography*, *52*(6), 2641–2655. https://doi.org/10.4319/lo.2007.52.6.2641

Smyth, W. D. (2020). Marginal instability and the efficiency of ocean mixing. *Journal of Physical Oceanography*, *50*(8), 2141–2150. https://doi.org/10.1175/JPO-D-20-0083.1

Smyth, W. D., & Moum, J. N. (2000a). Anisotropy of turbulence in stably stratified mixing layers. *Physics of Fluids*, *12*(6), 1343–1362. https://doi.org/10.1063/1.870386

Smyth, W. D., & Moum, J. N. (2000b). Length scales of turbulence in stably stratified mixing layers. *Physics of Fluids*, *12*(6), 1327–1342. https://doi.org/10.1063/1.870385

Sommer, T., Carpenter, J. R., Schmid, M., Lueck, R. G., & Wüest, A. (2013). Revisiting microstructure sensor responses with implications for double-diffusive fluxes. *Journal of Atmospheric and Oceanic Technology*, *30*(8), 1907–1923. https://doi.org/10.1175/JTECH-D-12-00272.1

Steinbuck, J. V., Stacey, M. T., & Monismith, S. G. (2009). An evaluation of $\chi_T$ estimation techniques: Implications for Batchelor fitting and $\varepsilon$. *Journal of Atmospheric and Oceanic Technology*, *26*(8), 1652–1662. https://doi.org/10.1175/2009JTECHO611.1

Thorpe, S. A. (2007). *An introduction to ocean turbulence*. Cambridge University Press. https://doi.org/10.1017/CBO9780511801198

Thorpe, S. A., Lemmin, U., Perrinjaquet, C., & Fer, I. (1999). Observations of the thermal structure of a lake using a submarine. *Limnology & Oceanography*, *44*(6), 1575–1582. https://doi.org/10.4319/lo.1999.44.6.1575

Troy, C., Cannon, D., Liao, Q., & Bootsma, H. (2016). Logarithmic velocity structure in the deep hypolimnetic waters of Lake Michigan. *Journal of Geophysical Research: Oceans*, *121*(1), 949–965. https://doi.org/10.1002/2014JC010506

Umlauf, L., & Lemmin, U. (2005). Interbasin exchange and mixing in the hypolimnion of a large lake: The role of long internal waves. *Limnology & Oceanography*, *50*(5), 1601–1611. https://doi.org/10.4319/lo.2005.50.5.1601

Van Haren, H. (2018). Philosophy and application of high-resolution temperature sensors for stratified waters. *Sensors*, *18*(10), 3184. https://doi.org/10.3390/s18103184

Van Haren, H., Piccolroaz, S., Amadori, M., Toffolon, M., & Dijkstra, H. A. (2021). Moored observations of turbulent mixing events in deep Lake Garda, Italy. *Journal of Limnology*, *80*(1), 1983. https://doi.org/10.4081/jlimnol.2020.1983

Webb, D. C., Simonetti, P. J., & Jones, C. P. (2001). Slocum: An underwater glider propelled by environmental energy. *IEEE Journal of Oceanic Engineering*, *26*(4), 447–452. https://doi.org/10.1109/48.972077

Wenegrat, J. O., & Thomas, L. N. (2020). Centrifugal and symmetric instability during Ekman adjustment of the bottom boundary layer. *Journal of Physical Oceanography*, *50*(6), 1793–1812. https://doi.org/10.1175/JPO-D-20-0027.1

Wüest, A., & Lorke, A. (2003). Small-scale hydrodynamics in lakes. *Annual Review of Fluid Mechanics*, *35*(1), 373–412. https://doi.org/10.1146/annurev.fluid.35.101101.161220

Wüest, A., Piepke, G., & Van Senden, D. C. (2000). Turbulent kinetic energy balance as a tool for estimating vertical diffusivity in wind-forced stratified waters. *Limnology & Oceanography*, *45*(6), 1388–1400. https://doi.org/10.4319/lo.2000.45.6.1388

Wüest, A., Van Senden, D. C., Imberger, J., Piepke, G., & Gloor, M. (1996). Comparison of diapycnal diffusivity measured by tracer and microstructure techniques. *Dynamics of Atmospheres and Oceans*, *24*(1–4), 27–39. https://doi.org/10.1016/0377-0265(95)00408-4

## References From the Supporting Information

Merckelbach, L. (2018). Initial release of Glider flight model. Version 1.0.1 [Software]. Zenodo. https://doi.org/10.5281/zenodo.2222694

## Erratum

After original publication of this article, Figures 2, 8, and 11 were resized in the PDF. This may be considered the authoritative version of record.